Contact-line dynamics of a diffuse fluid interface

By D A V I D J A C Q M I N

NASA Lewis Research Center, Cleveland, OH 44135, USA

An investigation is made into the moving contact line dynamics of a Cahn–Hilliard–van der Waals (CHW) diffuse mean-field interface. The interface separates two incompressible viscous fluids and can evolve either through convection or through diffusion driven by chemical potential gradients. The purpose of this paper is to show how the CHW moving contact line compares to the classical sharp interface contact line. It therefore discusses the asymptotics of the CHW contact line velocity and chemical potential fields as the interface thickness ϵ and the mobility κ both go to zero. The CHW and classical velocity fields have the same outer behaviour but can have very different inner behaviours and physics. In the CHW model, wall–liquid bonds are broken by chemical potential gradients instead of by shear and change of material at the wall is accomplished by diffusion rather than convection. The result is, mathematically at least, that the CHW moving contact line can exist even with no-slip conditions for the velocity. The relevance and realism or lack thereof of this is considered through the course of the paper.

The two contacting fluids are assumed to be Newtonian and, to a first approximation, to obey the no-slip condition. The analysis is linear. For simplicity most of the analysis and results are for a 90° contact angle and for the fluids having equal dynamic viscosity μ and mobility κ. There are two regions of flow. To leading order the outer-region velocity field is the same as for sharp interfaces (flow field independent of r) while the chemical potential behaves like $r^{-\xi}$, $\xi = \pi/2/\max\{\theta_{eq}, \pi - \theta_{eq}\}$, θ_{eq} being the equilibrium contact angle. An exception to this occurs for $\theta_{eq} = 90°$, when the chemical potential behaves like $\ln r/r$. The diffusive and viscous contact line singularities implied by these outer solutions are resolved in the inner region through chemical diffusion. The length scale of the inner region is about $10\sqrt{\mu\kappa}$ –typically about 0.5–5 nm. Diffusive fluxes in this region are $O(1)$. These counterbalance the effects of the velocity, which, because of the assumed no-slip boundary condition, fluxes material through the interface in a narrow boundary layer next to the wall.

The asymptotic analysis is supplemented by both linearized and nonlinear finite difference calculations. These are made at two scales, experimental and nanoscale. The first set is done to show CHW interface behaviour and to test the qualitative applicability of the CHW model and its asymptotic theory to practical computations of experimental scale, nonlinear, low capillary number flows. The nanoscale calculations are carried out with realistic interface thicknesses and diffusivities and with various assumed levels of shear-induced slip. These are discussed in an attempt to evaluate the physical relevance of the CHW diffusive model. The various asymptotic and numerical results together indicate a potential usefullness for the CHW model for calculating and modelling wetting and dewetting flows.

1. Introduction

The idea that a fluid–fluid interface is diffuse, that is, has finite thickness, goes back to Poisson (1831) and Gibbs (1876). Recently, diffuse interface modelling of multi-phase mixtures has become fairly popular, primarily because of its usefulness as a numerical device (Brackbill, Kothe & Zemach 1992; Unverdi & Tryggvason 1992; Lafaurie *et al.* 1994; Sussman, Smeraka & Osher 1994; Kothe *et al.* 1996) but also as a means to gain insight into the small-scale physics of fluids (Anderson & McFadden 1997). A review of much of this recent work is given by Anderson, McFadden & Wheeler (1998).

Van der Waals (1893) introduced the first and probably still most used diffuse interface model. Following Cahn (1961), it has been extensively used in the study of the diffusion-dominated evolution of interfaces. The model's application to fluid dynamics has been recently proposed and discussed by Antanovskii (1995), Gurtin, Polignone & Viñals (1996), Nadiga & Zaleski (1996), Anderson & McFadden (1997), and Jacqmin (1996), among others, and it has been used in numerical calculations of fluid mechanical problems by Jacqmin (1995, 1996), Chella & Viñals (1996), and Jasnow & Viñals (1996).

This discussion in the main part of this paper is restricted to incompressible fluids. The CHW (Cahn–Hilliard–van der Walls) model for this case takes the local free energy density in a two-component fluid to be a function not only of composition but also a quadratically increasing function of the local composition gradient. Infinitely sharp interfaces are therefore forbidden. Van der Waals introduced the model in order to discuss equilibrium fluid–fluid interfaces and to illustrate how and why these interfaces have surface tension. The width, profile and surface tension of a CHW interface in equilibrium is determined by the minimization of the free energy of the interface.

If a CHW interface is not in equilibrium then two mechanisms exist to equilibrate it. The first mechanism is diffusional: gradients of chemical potential can induce countercurrents of the fluid's two components. These can bring an interface to its proper profile and, at micron-scale curvatures and below, even move an interface. The second mechanism is advective: gradients of chemical potential produce surface tension forcing of fluid momentum. The CHW model is similar to and a simplification of van der Waals mean-field models of intermolecular forcings. For example, like mean-field models based on Lennard–Jones integrals, the CHW model can be used to model disjoining pressure effects. Because the CHW model includes diffusion it can be used not only to examine interfacial instabilities due to disjoining pressures but also any subsequent dissolution/solution of one fluid into the other.

A potential major application of continuum interface models is to the resolution of the various flow singularities that arise from the classical sharp-interface treatment of fluids. These include topological/stress singularities arising from droplet coalescences and breakups (Lowengrub & Truskinovsky 1998). These problems are of basic physical interest in themselves but they are also highly relevant to the question of the accuracy of numerical methods that use diffuse interfaces.

This paper examines the applicability of the CHW model to moving contact lines. Two points of view are taken, corresponding to two different meanings of 'applicability'. The first question is: is the CHW model useful? The second question is: are results from the CHW model relevant to real contact line physics? The answers to both questions depend heavily on how the CHW model handles and resolves the well-known inner-region contact-line singularity. Much of this paper therefore

concentrates on elucidating the asymptotic, small-scale structure of the CHW contact line region.

The analysis in the paper is for a two-component, two-phase, incompressible fluid system that obeys the Navier–Stokes equations with Newtonian stresses and that, to a first approximation, obeys the no-slip boundary condition on walls. The usual contact line model takes the fluid–fluid interface to be sharp and to be a material interface, i.e. there is no flux through it. The further imposition of the no slip boundary condition then leads to a contradiction: the flow field at the contact line is multi-valued and the total shear force is logarithmically singular.

The obvious path to resolve the contradiction is to allow some slip, in, for example, a small region surrounding the contact line, or equal to wall shear stress times a small parameter. The physical import of shear-induced slip, as pointed out by Durbin (1988), is that viscous transfer of momentum can break fluid–wall molecular bonds, allowing the contact line to move.

The CHW model allows a different resolution. This resolution is possible – at least, mathematically – even when perfect no-slip is assumed. The CHW interface is not a material line and it can be moved diffusively as well as by advection. With no-slip, Cahn–Hilliard chemical potential gradients right at the moving contact line become such that diffusive fluxes there are $O(1)$. These fluxes are competitive with convective transport. Together with a diffusive wall boundary condition they allow the contact line to be moved while simultaneously maintaining the diffuse interface's form and stability. The physical import of the diffusive boundary condition is that fluid–wall molecular bonds are broken by potential energy related forces.

The CHW model appears to hold great promise (Jacqmin 1999) for numerical applications; its diffuse interface allows the use of numerical methods that are more general and powerful, though admittedly less accurate, than are available for sharp interfaces. It can also be useful for analytic studies of two-phase flows involving diffusive interfacial mass transfer, nucleation or dissolution, or disjoining pressures. The question of its usefulness for moving contact line analyses comes down to the details of how the CHW model resolves the contact line singularity. The first sub-question is whether the resolution leads to correct macroscopic results. As expected from Cox's (1986) analysis, the answer is yes. The second sub-question is how this resolution behaves asymptotically. This must be known in order to understand and test non-asymptotic numerical or analytic CHW contact-line results or, when developing numerical methods, to establish paths to numerical convergence. The paper discusses some experimental-scale numerical calculations to show how results from the asymptotic theory can be useful in understanding finite Reynolds number, macroscopically thick, numerical interfaces.

The question of the physical relevance of the CHW diffusive resolution of the contact-line singularity is difficult. It seems certain that some such effects must occur. The high curvature of the interface near the contact line should affect the phase behavior, meaning the mutual solubility and the density, of the fluids there. The amelioration of high curvatures through diffusion is well known in crystal growth and equation systems similar to the Cahn–Hilliard equation have had success in modelling it. However, it turns out that for moving contact lines these effects become important only at very small scales. The diffusive length scale of the CHW contact line will be shown to be $\sqrt{\mu\kappa}$, where μ is dynamic viscosity and κ is mobility. For a 90° equilibrium contact angle the inner region – the region where the flow field is significantly affected by chemical potential gradients – is about ten times this length scale. κ in liquids is typically about 10^{-14}, in units of $cm^5 s^{-1} erg^{-1}$. This results in a diffusive length scale

of somewhere between 1 Å and 1 nm and an inner region of 1–10 nm. The size of small molecules is about 3 Å and interface thickness itself is about 1 nm. The CHW theory applied to moving contact lines may thus be mildly inconsistent in that to the degree it is applicable, or, at least, pointing in the right direction, it also calls for a more careful consideration of subcontinuum effects, particularly the details of wall–liquid molecular interactions, that it does not include. Also, at these scales it may not be reasonable to assume shear stress/slip effects are negligible. An attempt will be made in § 11 to evaluate chemical potential/diffusive versus shear stress effects with some nanoscale calculations. These have been made with realistic diffusivities and interface thicknesses and with various assumed levels of shear-induced slip.

Previous work in this area has been done by Seppecher (1996), who has presented an analysis and some microscale calculations of diffuse contact lines in a model compressible fluid. The Appendix discusses his work further. Works related to chemical potential forcing of contact line flows include de Gennes, Hua & Levinson (1990), who discuss the effect of van der Waals forces on low- or high-angle (near 0° or 180°) moving contact lines; Blake (1993), who hypothesizes that activation free energies involved in breaking wall–liquid bonds are important in setting wetting rates; Miller & Ruckenstein (1974) and Lopez, Miller & Ruckenstein (1976), who discuss and evaluate van der Waals forcings of wetting fluid flows, as do Li & Slattery (1991); Indeikina & Chang (1998), who discuss van der Waals forcings in contact line movement of partially wetting fluids; and Wayner & Schonberg (1992), who discuss spreading of a liquid film through evaporation and condensation caused by chemical potential differences.

The following analysis and calculations will use the simplest possible Navier–Stokes/CHW diffuse-interface flow model; they use a single composition variable and, as mentioned above, the equations are incompressible. These simplifications result in the neglect of some important effects. First, it would be better to represent the system using two composition variables. Each could then diffuse independently and each could vary independently in interfacial regions. Second, the neglect of compressibility means that the chemical potential is a function only of mole or mass fractions rather than densities. This analysis is most most likely to be physically relevant to liquid–liquid systems where there is some degree of solubility between the two components and where the solubility is a function of chemical potential. Also, because of air's relatively high volumetric solubility and diffusivity in liquids, it may have qualitative relevance to air/liquid systems.

2. The diffuse interface Navier–Stokes equations

An interface's thickness and the composition profile through the interface are set by the competition between random molecular motion (thermal motion) and molecular attractions. Van der Waals (1893) modelled this competition by introducing a free energy density dependent on both composition and composition gradients:

$$f = \tfrac{1}{2}\epsilon\sigma\alpha|\nabla C|^2 + \epsilon^{-1}\sigma\beta\Psi(C). \tag{2.1}$$

Here, f is the free energy per volume and C is a 'measure' of phase. The first term in (2.1) is the energy density due to phase gradients and the second is the bulk energy density. $\Psi(C)$ models the fluid components' immiscibility and has two minima corresponding to the fluid's two stable phases. Van der Waals hypothesized that equilibrium interface profiles are those that minimize the free energy $\mathscr{F} = \int f \, dV$.

From the calculus of variations, these profiles satisfy

$$\epsilon\sigma\alpha\nabla^2 C - \epsilon^{-1}\sigma\beta\Psi'(C) = -\phi = \text{const.}; \tag{2.2}$$

where $\phi \equiv \delta\mathscr{F}/\delta C$ is the fluid's chemical potential. Equation (2.2) yields interfaces with surface tension σ and interface thickness ϵ; α and β are dimensionless $O(1)$ constants determined by the choice of Ψ and by a chosen definition of interface thickness. The surface tension is equal to the integral of the free energy density through the interface per unit area. For a flat interface with equilibrium profile $C = C(y)$ the surface tension is given by the integral

$$\sigma = \epsilon\sigma\alpha \int_{-\infty}^{+\infty} \left(\frac{\partial C}{\partial y}\right)^2_{\text{eq}} \mathrm{d}y. \tag{2.3a}$$

In other words,

$$\epsilon\alpha \int_{-\infty}^{+\infty} \left(\frac{\partial C}{\partial y}\right)^2_{\text{eq}} \mathrm{d}y = 1. \tag{2.3b}$$

This determines α from a given profile.

Cahn (1961) extended van der Waals' hypothesis to time-dependent situations by approximating interfacial diffusion fluxes as being proportional to chemical potential gradients. The Cahn–Hilliard equation

$$\frac{\partial C}{\partial t} = \kappa\nabla^2\phi = -\kappa\nabla^2(\epsilon\sigma\alpha\nabla^2 C - \epsilon^{-1}\sigma\beta\Psi'(C)) \tag{2.4}$$

models the creation, movement, and dissolution of diffusively controlled phase interfaces (Bates & Fife 1993); κ is called the *mobility*. The bulk phase chemical *diffusivity* is given by $\epsilon^{-1}\sigma\beta\kappa\Psi''(C_{\text{bulk phase}})$. The free energy of a system determined by (2.4) decays monotonically:

$$\frac{\mathrm{d}\mathscr{F}}{\mathrm{d}t} = -\kappa \int (\nabla\phi)^2 \, \mathrm{d}V. \tag{2.5}$$

The further extension of the van der Waals model to advection problems has been recently carried out by, among others, Antanovskii (1995), Jacqmin (1995, 1996), Chella & Viñals (1996), Nadiga & Zaleski (1996), and Anderson & McFadden (1997). Advection can change free energy but must leave the total energy of a fluid unchanged. The compensatory forcing of momentum by the free energy field must therefore be $F_i = -\delta\mathscr{F}/\delta u_i = -C\nabla\phi$ (Jacqmin 1996, 1997). A CHW two-phase, viscous, incompressible fluid obeys

$$\frac{\mathrm{D}C}{\mathrm{D}t} = \kappa\nabla^2\phi = -\kappa\nabla^2(\epsilon\sigma\alpha\nabla^2 C - \epsilon^{-1}\sigma\beta\Psi'(C)), \tag{2.6}$$

$$\rho(C)\frac{\mathrm{D}u_i}{\mathrm{D}t} = -\nabla S + \nabla \cdot \tau_{\text{visc},i} - C\nabla\phi, \tag{2.7}$$

$$\sum_i \frac{\partial u_i}{\partial x_i} = 0. \tag{2.8}$$

This gives the *potential* form of the surface tension forcing. S enforces incompressibility. (However, it is not the pressure.) The $\tau_{\text{visc},i}$ are the viscous stresses. A *stress* form of the surface forcing also exists. The momentum equations become

$$\rho(C)\frac{\mathrm{D}u_i}{\mathrm{D}t} = -\nabla p + \nabla \cdot \tau_{\text{visc},i} + \sum_j \frac{\partial \tau_{ij}}{\partial x_j}, \tag{2.9}$$

where the surface stresses are

$$\tau_{jj} = \epsilon\sigma\alpha \sum_{i \neq j} \left(\frac{\partial C}{\partial x_i}\right)^2, \tag{2.10}$$

$$\tau_{ij,i \neq j} = -\epsilon\sigma\alpha \left(\frac{\partial C}{\partial x_i}\frac{\partial C}{\partial x_j}\right), \tag{2.11}$$

and p is the pressure.

The viscous boundary condition used in most of this paper and for all the asymptotic theory is no slip. Two boundary conditions are needed for C. The no-flux condition for C is

$$\frac{\partial \phi}{\partial x_n} = 0. \tag{2.12}$$

The second boundary condition depends on the interface at the wall being at or near local equilibrium. Postulating that the wall free energy is of the form

$$\mathscr{F}_w = \int \gamma g(C)\,\mathrm{d}A, \tag{2.13}$$

that is, that the wall–fluid interfacial energy is a function only of the the fluid composition right against the wall, then the resulting natural boundary condition, which corresponds to a diffusively controlled local equilibrium at the wall, is

$$\epsilon\sigma\alpha\frac{\partial C}{\partial x_n} + \gamma g'(C) = 0, \tag{2.14}$$

where x_n is the direction normal to and into the wall. Equation (2.14) is analogous to the classical contact angle condition in which the dynamic contact angle right at the wall (the microscopic contact angle) is taken to be the same as the static equilibrium angle. When $g(C)$ is zero the equilibrium contact angle is 90°. A more general condition that allows non-equilibrium is

$$\frac{\mathrm{D}C}{\mathrm{D}t} = D_w \left(\epsilon\sigma\alpha\frac{\partial C}{\partial x_n} + \gamma g'(C)\right). \tag{2.15}$$

This results in the microscopic contact angle being a function of wall velocity. C approaches the equilibrium condition as D_w increases to infinity. In the following analysis D_w will be assumed to be at least $O(1/\epsilon)$. Then $\epsilon\sigma\alpha D_w$ is at least $O(1)$† and perturbations to the microscopic contact angle caused by low-capillary-number contact line movement are, it will be shown, $O(Ca)$, where Ca is the capillary number, or smaller.

At this point, some discussion is needed about the physical meaning of the no-slip condition. The reader has already been alerted (§ 1) that diffusive fluxes along the wall in the vicinity of a moving contact line will be found to be $O(1)$. It may thus seem unreasonable that convection there is forced in this analysis to equal the wall speed. Since the diffusion 'flow' seems to slip, why not the velocity?

† The assumption is justified by recent molecular dynamics calculations of fluid equilibration against walls (Matsumoto, Maruyama & Saruwatari 1995; Wagner 1995) that indicate fluid–wall equilibration times that are sub-nanosecond. Since $\epsilon\sigma\alpha\partial C/\partial x_n$ and $\gamma g'(C)$ are each $O(1)$, matching this in (2.15) requires a D_w of about 10^9. Fluid–fluid interfaces away from critical points are typically nanometers wide, indicating an $\epsilon\sigma\alpha$ of about 10^{-7}. The choice $\epsilon\sigma\alpha D_w \geqslant O(1)$ thus seems relevant and physically reasonable. An exception to this general argument might be when the wall bonds of the displaced fluid are very strong and thus, perhaps, slow to break.

A partial answer to this is that the diffusive flux is not a coherent, macroscopic flow but is better viewed – at least for a small-molecule liquid–liquid system – as being made up of numbers of microscopic-scale interchanges of molecular positions. The result is two opposing countercurrents, one of one material, one of the other. At the wall itself, these interchanges can be modelled as site interchanges: a molecule of one fluid phase exchanges a wall site with a molecule of another phase, or a molecule in the interior of the fluid grabs a wall site from a fluid molecule attached to the wall (Blake 1993). These interchanges will tend to be energy downgradient, and their general direction will be in response to changes in the surrounding fluid environment. The energy required to make the interchanges is provided by random thermal motion.

In contrast, a slip velocity would involve a large-scale breaking of bonds with no compensating release of free energy, as most of the convection would involve the replacement at wall sites of like molecules by like. The exception to this is if slip occurs only in the immediate vicinity of the contact line.

A hybrid model (Blake) is chemical-potential-gradient-induced slip:

$$(u_j - U_j) \propto \left(\epsilon \sigma \alpha \frac{\partial C}{\partial x_n} + \gamma g'(C) \right) \frac{\partial C}{\partial x_j}, \qquad (2.16)$$

where U_j is the jth velocity component of the wall and $u_j - U_j$ is the slip velocity. This slip velocity is proportional to the wall shear stress caused by chemical potential. This allows slip only in the interface itself, is thus of very small scale, and would be energy efficient.

The coexistence of no slip with along-wall diffusion is supported by at least two molecular dynamics studies. Thompson & Robbins (1990) have carried out molecular dynamic calculations of very small-scale Couette flow driven by crystalline walls. They found, when wall molecule spacing and fluid molecule/fluid molecule separations are roughly commensurate, that no slip occurs at a fairly low wall–fluid interaction energy. At low and moderate wall-fluid energy the diffusion rate along the wall is essentially the same as in the interior. They found that a high liquid–wall interaction energy (1.8 times that of the liquid–liquid interaction) was necessary before the near-wall liquid solidified and self-diffusion was cut off. Koplik & Banavar (1998) have looked at two-component nanoscale plane Poiseuille flow. The two components were miscible. Though one of the components had a fairly weak wall interaction, they found that each material individually obeyed the no-slip condition. They wrote: 'The molecular origin of no slip is that fluid molecules near the wall are, on the one hand, dragged along in the direction of the net flow by their neighbors further away from the wall, and, on the other hand, are pushed up against the wall by the crowding of molecules in a dense liquid, where they interact with the effectively corrugated potential of the wall. While the molecules are not literally stuck there, their translation speed is much reduced as they interact with the almost-fixed wall atoms, and a typical trajectory is a random walk with a drift in the direction of the applied force.'

Following Durbin (1988), it is possible to estimate the shear required for contact-line slip from (more-or-less) first principles. This is done by finding the rate of work needed to break or partially break wall–liquid bonds. Wall–liquid bonds have roughly the same strength as liquid–liquid bonds, which in turn have about the same energy as fluid–fluid surface energy (which indicates the energy needed for breaking of these bonds). A typical wall–liquid bonding energy is from about 5–50 erg cm^{-2}. The estimate of shear needed assumes that any slip would involve near-wall molecules that would be generally trapped close to the wall by other liquid molecules and that,

as a result, their slip would require repeated movement from favourable near-wall locations to unfavourable ones and back again. Each traversal of an energy barrier would then give an energy dissipation that would be a significant fraction of the wall–liquid bond strength–that is, it would essentially involve the partial breaking and then remaking of a wall–liquid bond, in the course of this turning some work into heat. It also assumes that wall molecule spacing and fluid molecule/fluid molecule separations are roughly the same. The power per area needed to continuously break wall–liquid bonds in this way is $\lambda \sigma_{lw} V_{\mathrm{wall}}/4 \times 10^{-8}$, where σ_{lw} is the wall–liquid bonding energy and λ is the fraction of wall–liquid bond energy that is dissipated at each traversal. The assumed intermolecular spacing is 4×10^{-8} cm and $V_{\mathrm{wall}}/4 \times 10^{-8}$ is the rate of wall–liquid bond breaking at a particular location per second. The rate of work per area done by shear stress is approximately equal to $\mu V_{\mathrm{wall}}^2/L$, where L is the slip length (the near-contact-line inner scale) at the contact line and μ is the dynamic viscosity. The work done and energy needed must be equal, giving an L of about $4 \times 10^{-8} \mu V_{\mathrm{wall}}/\lambda \sigma_{lw} = 4 \times 10^{-8}(1/\lambda)(\sigma/\sigma_{lw})\, Ca$. For a σ/σ_{lw} of about 2, a fairly typical liquid–liquid capillary number of about 0.01, and assuming a λ of about 0.05, this gives a slip length of about 2 Å.

This estimate appears to be in good agreement with molecular dynamics calculations of contact line flow. Results of Koplik, Banavar & Willemsen (1989) and Thompson & Robbins (1989) both indicate barely distinguishable, sub-continuum slip regions. Both these calculations are of liquid–liquid flow at $Ca \simeq 0.01$, with fairly strong wetting of the wall by both fluids.

Along the same lines, though in a different direction, Barrat & Bocquet (1999) have recently shown that non-wetting liquids can show much larger slip effects. This is because of reduced levels of wall–liquid bonding. They carried out molecular dynamics calculations of plane Poiseuille and Couette flow of liquids between walls for which the liquids had equilibrium liquid/vapour contact angles greater than 90°. They found slip lengths of about 6 Å for 100° contact angle fluid and about 3 nm for a 145° contact angle.

Section 11 will consider slip further. Nanoscale calculations will be discussed that include slip. Comparisons will be made between shear stresses and chemical potential forces at the contact line to try to determine when each is dominant.

3. Experiment-scale calculations of CHW contact lines

The purpose of this section is to motivate the asymptotic analysis by first showing the reader some 'practical' experimental-scale computational results. The interfaces in these calculations are much wider than in reality but calculations using them can nevertheless be qualitatively useful and they show the main features of diffuse-interface asymptotic behaviour. The calculations are of the full nonlinear equations (2.6)–(2.8) with Newtonian stresses and using the no-slip boundary condition. Some of the important characteristics of CHW contact lines that are shown in this section are (i) the CHW moving contact line is stable and stops most through-flow even with no-slip conditions, (ii) through-flow is reduced as the interface becomes thinner, (iii) the chemical potential field scales differently from interface thickness, and (iv) the distortion of the interface profile due to convection becomes smaller as the interface becomes thinner.

Even very crude calculations of the CHW diffuse-interface model seem to give the essentials of what is known about dynamic contact lines. Figure 1 shows an axisymmetric 'gas'–liquid dynamic contact line in a steady frame of reference. The
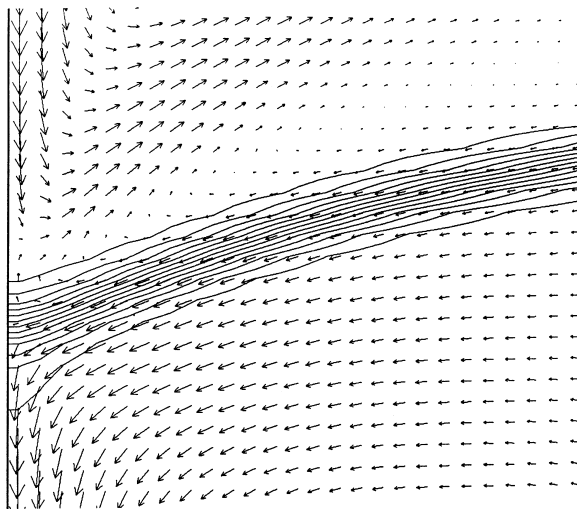
FIGURE 1. Steady flow pattern at a diffuse-interface contact line. The upper fluid has one-hundredth the density and one-thousandth the viscosity of the lower fluid.

'gas' has a specific density of 0.01, the liquid 1.00; the gas has one-thousandth the viscosity of the liquid. The figure shows contours of the diffuse interface with the velocity vector field superimposed; $g(C)$ was set equal to zero. Equation (2.14) was used for the C boundary condition so the meniscus right at the wall comes in at the equilibrium 90° angle.

What is remarkable is the way the diffuse interface forces seem to almost completely stop the downward motion of fluid just at the contact line. The computation was made using a staggered grid so the leftmost vertical velocity that is shown is actually 1/2 grid cell from the true boundary. The computation is no slip in the sense that the assigned wall velocity is used to compute the viscous shear forces on the leftmost velocity. This condition is not relaxed at the meniscus. To within the resolution of the computation the vertical flow in the cells next to the contact line appears to stop, but just above and below the meniscus the flow is very close to wall speed.

The flow away from the contact line agrees in character with the wedge flow solution of Huh & Scriven (1971). The gas, which is the upper fluid, is swept down with the moving boundary but when it reaches the contact line it is forced out in a jet at about a 30° angle to the meniscus. The viscous liquid flow is entrained along the meniscus into the wall flow. The reversal of flow from outgoing gas to ingoing liquid takes place in a thin boundary layer in the gas just above the meniscus.

Figures 2–5 show a set of calculations of a liquid–liquid meniscus in a driven cavity. The calculations are of the full nonlinear equations. In order to isolate surface tension effects, the two liquids were given the same density and viscosity. For symmetry, the driven cavity was given two moving walls: the left wall is downward moving, the right wall upward. The cavity size is 2 by 6 cm, wall speed is $0.4 \, \mathrm{cm \, s^{-1}}$, the surface tension is 30 erg $\mathrm{cm^{-2}}$, the viscosity is 1 P $(1 \, \mathrm{g \, cm^{-1} \, s^{-1}})$, and the specific gravity is 1. The capillary number, $\mu V_{\mathrm{wall}}/\sigma$, of the flow is 0.01333. $\Psi(C)$ is modelled as $(C - 1/2)^2(C + 1/2)^2$. The equilibrium interface for this has a tanh profile and ϵ is defined to be the distance through the interface from $C = -0.45$ to $+0.45$. From Ψ, equation (2.3b) and this definition, $\alpha = 3/(2 \tanh^{-1}(0.9)) \simeq 1.019$ and $\beta = 12 \tanh^{-1}(0.9) \simeq 17.667$. The equation for the equilibrium profile is $C = \frac{1}{2} \tanh(\zeta)$,
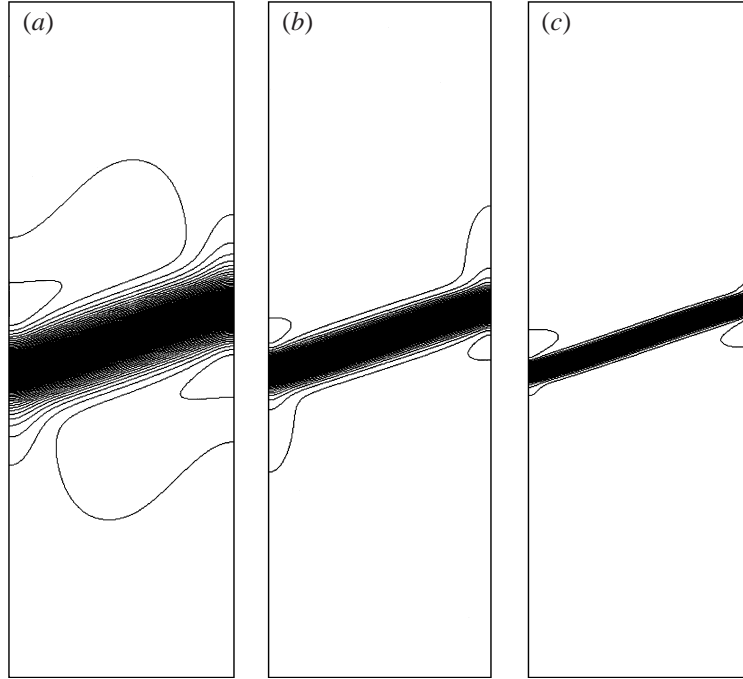
FIGURE 2. The meniscus for the double-contact-line computation for three meniscus widths. Contours of C are shown, for C from $-1/2$ to $+1/2$, at intervals of 0.01. The fluids above and below the interface have identical densities and viscosities. The perturbation to interface structure becomes smaller as the interfaces become thinner.

where $\zeta = \epsilon^{-1}\sqrt{\beta/2\alpha}\, y = 2\epsilon^{-1}(\tanh^{-1} 0.9)\, y$. Figure 2 shows the meniscus for three different interface widths: the width in (*b*) is half that of (*a*), and in (*c*) half that of (*b*); ϵ for the thickest interface is 0.6475 cm. The mobility κ was kept proportional to the interface width so it too gets successively smaller. It is $2.65 \times 10^{-5}\,\mathrm{cm}^5\,\mathrm{s}^{-1}\,\mathrm{erg}^{-1}$ for the thickest interface. The equilibrium condition (2.14) with $g' = 0$ was used for the C boundary condition.

Comparing figures 2(*a*)–2(*c*) we see that the interface becomes noticeably less distorted as it becomes thinner. The source of the distortion is that there is some flow through the meniscus next to the wall and this tends to drag the meniscus down with it. But chemical diffusion limits the effects of this drag–the molecules of the upper fluid migrate diffusively back to it. The interface is dragged down less as the interface thins because diffusion, with its time scale proportional to $O(\kappa/\epsilon^3)$, becomes increasingly dominant over convection with its time scale of $O(\epsilon^{-1})$.

Figure 3 compares menisci centrelines. These are nearly identical, with a slight increase of slope as the interface becomes thinner. The menisci are nearly straight except right at the contact lines, where they curve in very sharply to the equilibrium angle. The averaged slope of the thickest meniscus is 0.2842: the medium meniscus has a slope of 0.2873, the thinnest a slope of 0.2972. The maximum slope (at the box midpoint) of the thickest meniscus is about 0.331, of the thinnest about 0.336.

Figure 4 shows the stream function for each calculation. This shows some flow through the menisci right at the contact lines but this flow becomes much narrower and has much less volume as ϵ and κ are reduced. The coarsest calculation also
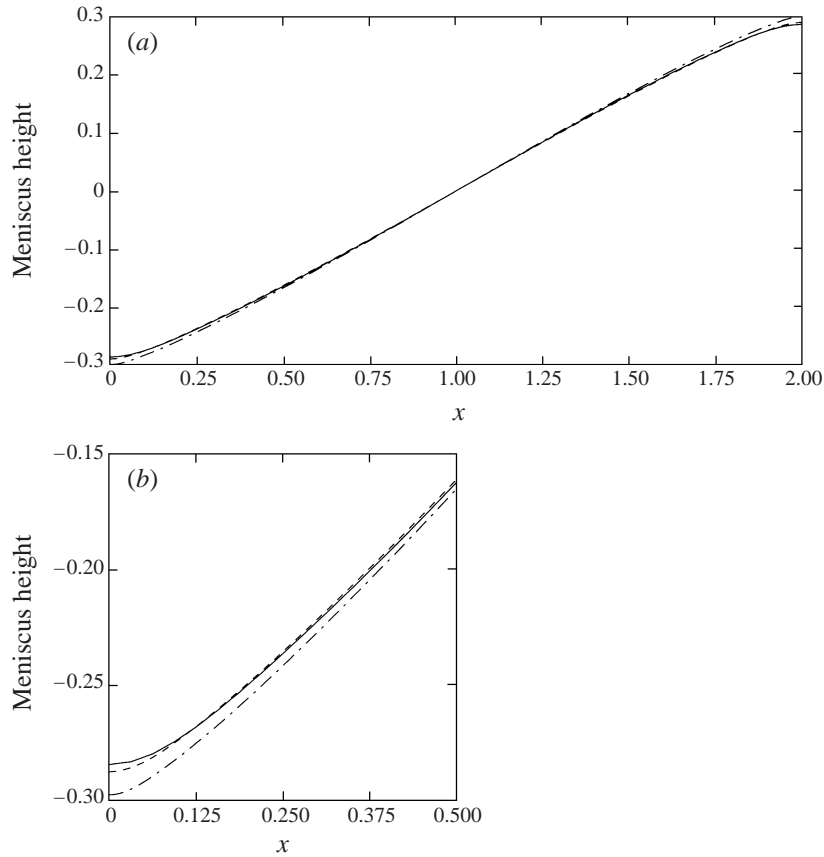
FIGURE 3. The meniscus centreline for the menisci shown in figure 2. The solid line is for the thickest meniscus, the dashed line for the intermediate, and the dashed-dotted line for the thinnest. (*b*) A closeup at the left contact line.

shows a noticeable amount of return flow. This return flow is also present in the finer calculations.

Figure 5 shows the chemical potential field for each calculation. The field shows a 'half-dumbbell' pattern about the contact lines but the size and intensity of this pattern changes with ϵ and κ. It roughly halves in size between (*a*) and (*c*). The chemical-potential length scale thus decreases more slowly than the interface thickness. The maximum value of the potential roughly doubles, from 84.1 to 187.7 erg cm^{-3}. The length scale of the near-contact-line potential field is approximately proportional to $\sqrt{\kappa}$ and its intensity to $1/\sqrt{\kappa}$. The diffusive fluxes at the contact line, which are proportional to κ times the magnitude of the potential divided by the length scale, have approximately the same maximum intensity for all three interface widths.

Figure 6 shows the fine calculation potential in detail. The potential pattern is centred on the contact line (not shown). As the contact line is approached the potential pattern is increasingly dominated by diffusive as opposed to convective effects; hence its increasing symmetry. The dumbbell pattern will be shown later to correspond to a logarithmic term in the asymptotic solution that has zero amplitude in the meniscus region but is large at the walls.
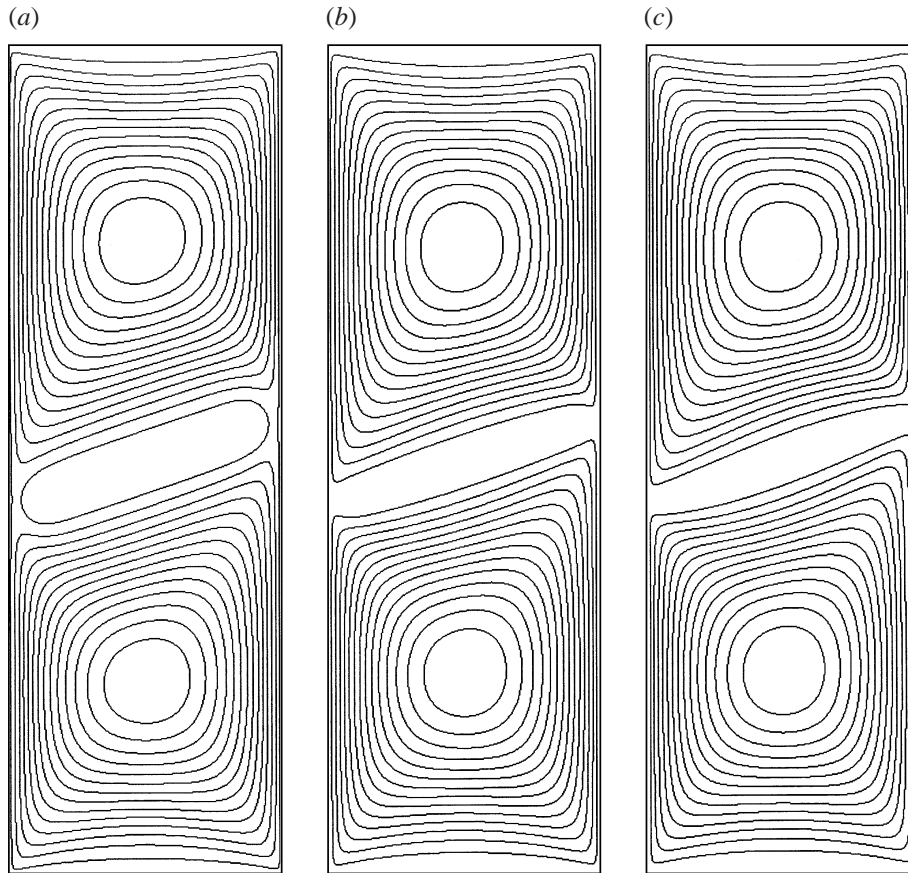
(a) (b) (c)

FIGURE 4. The stream function for the menisci shown in figure 2: (*a*) for the thickest meniscus shows the most through-flow at the moving wall.

4. The linearized equations for 90° contact angle

We now seek to develop an analytic theory for the CHW contact line. The case of a 90° equilibrium contact angle will be investigated first. To connect results to sharp-interface Navier–Stokes theory the analysis is for ϵ and κ asymptotically approaching 0. The situation that will be considered is that of a semi-infinite horizontal interface bounded by a vertical wall. The wall is moving downward at a very low speed. It is assumed, following Cox (1986), that the resulting flow can be analysed using linearized equations and that the wall velocity is low enough so that the asymptotics can be done using a two-region analysis. We seek to find the linearized steady-state solution for the resulting moving contact line flow, for the chemical potential, the interface slope, and for the perturbation to diffuse interface structure.

In order to analyse this dynamics in as simple a way as possible we consider, as in §3, a two-phase system in which the phases have the same viscosity and density. They are contained in a half-plane bounded by a vertical wall located at $x = 0$. This and the next few sections will consider the case of $g(C)$ constant. The equilibrium contact angle is then 90° and the equilibrium fluid interface obeys the one-dimensional
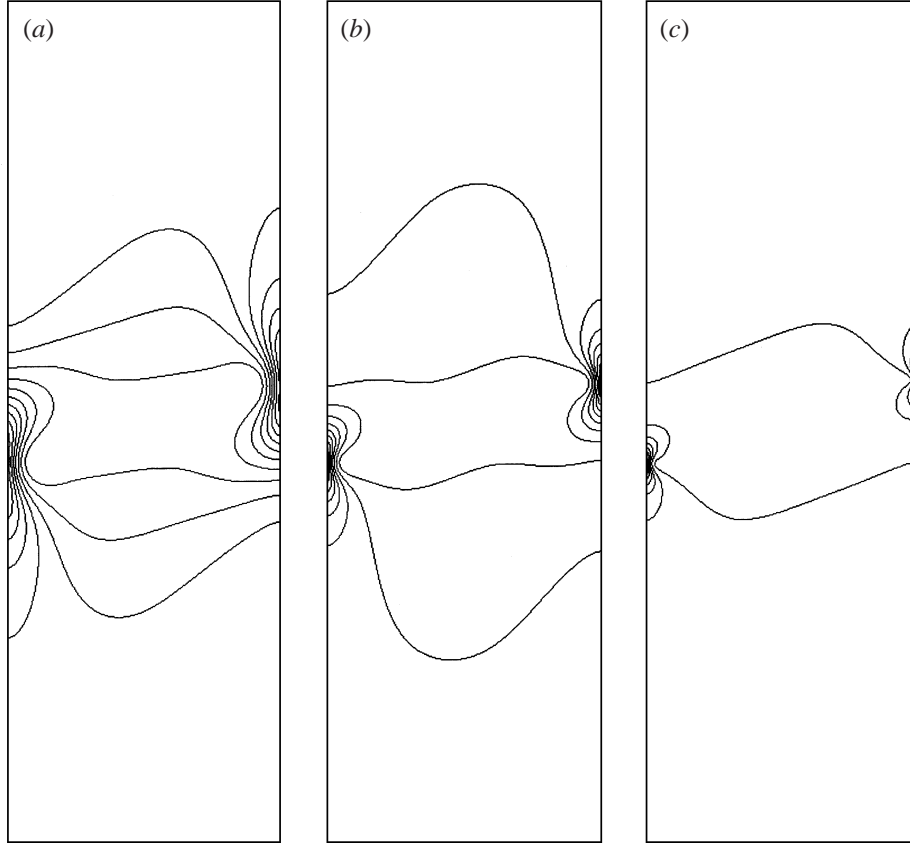
FIGURE 5. The chemical potential for the menisci shown in figure 2. The size of a chemical potential pattern near a contact line scales with $\sqrt{\kappa}$, its intensity scales as $1/\sqrt{\kappa}$.

equation

$$\epsilon\sigma\alpha\frac{\mathrm{d}^2\bar{C}}{\mathrm{d}y^2} - \epsilon^{-1}\sigma\beta\,\Psi'(\bar{C}) = 0. \tag{4.1}$$

The interface is centred on $y = 0$. The analysis will be for general $\Psi(\bar{C})$ except that Ψ is symmetric about $\bar{C} = 0$ and scaled so that $\bar{C}(\pm\infty) = \pm 1/2$. Because of Ψ's symmetry $\bar{C}$ is antisymmetric about $y = 0$.

Now consider the perturbation to this interface caused by the wall being set into very slow, steady, downward motion. The linearized, steady equations for this perturbation are

$$\kappa\nabla^2\phi = \bar{C}_y v, \tag{4.2}$$

$$\mu\nabla^2 u = \frac{\partial S}{\partial x} + \bar{C}\frac{\partial\phi}{\partial x}, \tag{4.3}$$

$$\mu\nabla^2 v = \frac{\partial S}{\partial y} + \bar{C}\frac{\partial\phi}{\partial y}, \tag{4.4}$$

$$\frac{\partial u}{\partial x} + \frac{\partial v}{\partial y} = 0, \tag{4.5}$$
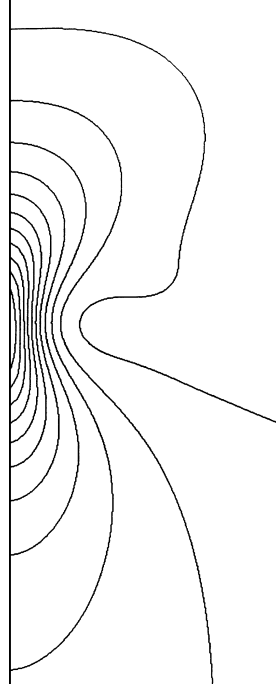
D. Jacqmin

FIGURE 6. A close-up at the left-hand contact line of the chemical potential shown in figure 5(*c*).

$$\epsilon\sigma\alpha\nabla^2 C - \epsilon^{-1}\sigma\beta\Psi''(\bar{C})C = -\phi, \tag{4.6}$$

$$u = 0, \quad v = -V_{\text{wall}}, \quad \frac{\partial\phi}{\partial x} = 0 \qquad \text{at } x = 0, \tag{4.7}$$

$$\epsilon\sigma\alpha D_w \frac{\partial C}{\partial x}\bigg|_{x=0} = \bar{C}_y v(x = 0) = -\bar{C}_y V_{\text{wall}}; \tag{4.8}$$

C and ϕ indicate perturbation quantities. Base-state quantities are indicated by overbars; μ is the dynamic viscosity.

Equations (4.2)–(4.8) decouple. The equations (4.2)–(4.5), (4.7) for the perturbation potential and the velocities are self-contained. C can be found separately from (4.6) and (4.8) after (4.2)–(4.5), (4.7) have been solved. Introducing the stream function ψ,

$$\partial\psi/\partial x = v, \quad \partial\psi/\partial y = -u, \tag{4.9}$$

the non-dimensionalization

$$\{x, y\} \rightarrow \sqrt{\mu\kappa}\{x, y\}, \quad \psi \rightarrow \sqrt{\mu\kappa}V_{\text{wall}}\,\psi, \quad \phi \rightarrow \sqrt{\mu/\kappa}V_{\text{wall}}\,\phi, \tag{4.10}$$

and noting that C, ϕ and ψ are symmetric about $y = 0$, the C and momentum equations become

$$\nabla^2\phi = \bar{C}_y \frac{\partial\psi}{\partial x}, \tag{4.11}$$

$$\nabla^2\nabla^2\psi = -\bar{C}_y \frac{\partial\phi}{\partial x}, \tag{4.12}$$

with the $x = 0$ boundary conditions:

$$\psi = 0, \quad \frac{\partial\psi}{\partial x} = -1, \quad \frac{\partial\phi}{\partial x} = 0, \tag{4.13}$$

and the $y = 0$ symmetry conditions:

$$\frac{\partial \psi}{\partial y} = \frac{\partial^3 \psi}{\partial y^3} = \frac{\partial \phi}{\partial y} = 0; \tag{4.14}$$

x, y, ψ, and ϕ now denote scaled quantities and $\bar{C}_y$ denotes the derivative of $\bar{C}$ with respect to scaled y.

5. The asymptotic form of the $\{\psi, \phi\}$ equations as $\epsilon/\sqrt{\mu\kappa} \to 0$

We now narrow consideration to the particularly simple case of $\epsilon/\sqrt{\mu\kappa} \to 0$. The case $\epsilon/\sqrt{\mu\kappa} = O(1)$ has the same asymptotic structure and gives essentially the same results. Adjustments needed to deal with this case will be discussed in § 8.

In the transformed coordinates the interface has thickness $O(\epsilon/\sqrt{\mu\kappa})$. This goes to zero as ϵ and κ go to zero provided that κ is $O(\epsilon^\delta)$, $\delta < 2$. The quantities ϕ and ψ are coupled only in the interfacial layer. If ϕ and ψ are slowly enough varying then the forcing terms $\bar{C}_y\{\partial\psi(x,y)/\partial x, -\partial\phi(x,y)/\partial x\}$ can be approximated by $\bar{C}_y\{\partial\psi(x,0)/\partial x, -\partial\phi(x,0)/\partial x\}$. In the limit of $\epsilon/\sqrt{\mu\kappa} \to 0$ these forcings become delta functions. Integrating (4.11) and (4.12) through the layer yields

$$\left.\frac{\partial \phi}{\partial y}\right|_{0_+} - \left.\frac{\partial \phi}{\partial y}\right|_{0_-} = \left.\frac{\partial \psi}{\partial x}\right|_0 \tag{5.1}$$

and

$$\left.\frac{\partial^3 \psi}{\partial y^3}\right|_{0_+} - \left.\frac{\partial^3 \psi}{\partial y^3}\right|_{0_-} = -\left.\frac{\partial \phi}{\partial x}\right|_0. \tag{5.2}$$

Because of the symmetry conditions at $y = 0$ these can be simplified to

$$\left.\frac{\partial \phi}{\partial y}\right|_{0_-} = -\frac{1}{2}\left.\frac{\partial \psi}{\partial x}\right|_0 \tag{5.3}$$

and

$$\left.\frac{\partial^3 \psi}{\partial y^3}\right|_{0_-} = \frac{1}{2}\left.\frac{\partial \phi}{\partial x}\right|_0. \tag{5.4}$$

The asymptotic form of equations (4.11)–(4.14) is thus

$$\nabla^2 \phi = 0, \tag{5.5}$$

$$\nabla^2 \nabla^2 \psi = 0, \tag{5.6}$$

$$\psi = 0, \quad \frac{\partial \psi}{\partial x} = -1, \quad \frac{\partial \phi}{\partial x} = 0 \quad \text{at } x = 0, \tag{5.7}$$

$$\frac{\partial \psi}{\partial y} = 0, \quad \frac{\partial^3 \psi}{\partial y^3} = \frac{1}{2}\frac{\partial \phi}{\partial x}, \quad \frac{\partial \phi}{\partial y} = -\frac{1}{2}\frac{\partial \psi}{\partial x} \quad \text{at } y = 0 \tag{5.8}$$

for the domain $x \geqslant 0$, $y \leqslant 0$.

6. Solution of the $\{\psi, \phi\}$ equations

The far-field solution consists of a forced component plus an infinite set of eigenfunctions. Schematically,

$$\phi = \phi_F + \sum E_n \phi_n, \quad \psi = \psi_F + \sum E_n \psi_n, \quad q = q_F + \sum E_n q_n, \tag{6.1}$$

where q is the vorticity. The eigenfunctions are of the form

$$\{\phi_n, \psi_n, q_n\} = \frac{1}{r^n}\left\{\sin n\theta, \; \frac{n+2}{n+1}\cos n\theta + \frac{n}{n+1}\cos(n+2)\theta, \; -\frac{4n}{r^2}\cos(n+2)\theta\right\} \quad (6.2)$$

for $n = 1, 3, 5 \ldots$. Here, $\theta = 0$ corresponds to the interface and $\theta = -\pi/2$ to the wall for $y \leqslant 0$. The eigenfunction amplitudes E_n are determined by matching to the inner flow. The forced component is the dominant far-field component. To leading order, the forced stream function is the wedge flow (Huh & Scriven 1971)

$$\psi_{F,0} = r\left(-A\sin\theta + A\theta\cos\theta + B\theta\sin\theta\right), \quad A = \frac{\frac{1}{2}\pi}{\left(\frac{1}{4}\pi^2 - 1\right)}, \quad B = -\frac{1}{\left(\frac{1}{4}\pi^2 - 1\right)}. \quad (6.3)$$

The leading-order vorticity is

$$q_{F,0} = \nabla^2\psi_0 = \frac{2}{r}(-A\sin\theta + B\cos\theta). \quad (6.4)$$

The leading-order potential has a term proportional to $\ln r/r$, plus $1/r$ terms:

$$\phi_{F,0} = -\frac{8}{\pi}A\frac{\ln r}{r}\sin\theta + \frac{4A}{r}\left(\frac{2}{\pi}\theta\cos\theta + \cos\theta\right); \quad (6.5)$$

$\phi_{F,0}$ in turn forces higher-order far-field terms in ψ_F and q_F. These are

$$\psi_{F,2} = -\frac{16}{\pi}A\frac{\ln r}{r}(\tfrac{3}{4}\cos\theta + \tfrac{1}{4}\cos 3\theta) + O\left(\frac{1}{r}\right), \quad q_{F,2} = \frac{32}{\pi}A\frac{\ln r}{r^3}\cos 3\theta + O\left(\frac{1}{r^3}\right). \quad (6.6)$$

Equations (6.3)–(6.6) approximate the far-field forced solution with a relative error of $O(1/r^2)$.

The near-field solution must be found numerically. Equations (5.5)–(5.8) have been solved using fourth-order-accurate finite differences and using the far-field solution as a boundary condition at finite r_{outer}. The accuracy and convergence of the calculated solution has been confirmed by calculating on progressively finer grids along with progressively greater values of r_{outer}. The eigenfunction amplitude E_1 was found to be about 10.53.

Figure 7 shows the near-field stream function (a) and chemical potential (b). Because the boundary condition is no slip, the velocity right next to the wall must be the same as that of the wall. An inner no slip boundary layer is shown. This inner layer, in which the velocity points downward though the interface, extends out to about $x = 5.1$. The amount of downward volume flux through the interface is about -1.55 (the value of the stream function at $x = 5.1$). Expressed in dimensional units this flux is $-1.55\sqrt{\mu\kappa}\,V_{\text{wall}}$, or $O(\sqrt{\mu\kappa})$. Past this inner no-slip boundary layer, the velocity through the interface is always upward. Its non-dimensional maximum value is 0.0618 at about $x = 9.5$.

The maximum value of the non-dimensional potential is found at the contact line and is about 1.84. Since this drops to near zero over a non-dimensional distance of $O(1)$ the non-dimensional diffusive flux is $O(1)$. The dimensional diffusive flux is given in terms of non-dimensional $\{x, y, z, \phi\}$ by $-V_{\text{wall}}\nabla\phi$ and is also $O(1)$ (or $O(V_{\text{wall}})$). The chemical potential obeys the jump condition (5.1) at the interface, hence the kinks in the contour lines there. The direction that a kink points to depends on the direction of the velocity there: to the right for downward flow, to the left for upward. The chemical potential in the outer regions of the plot is dominated by its $\sin\theta\ln r/r$ far-field term.
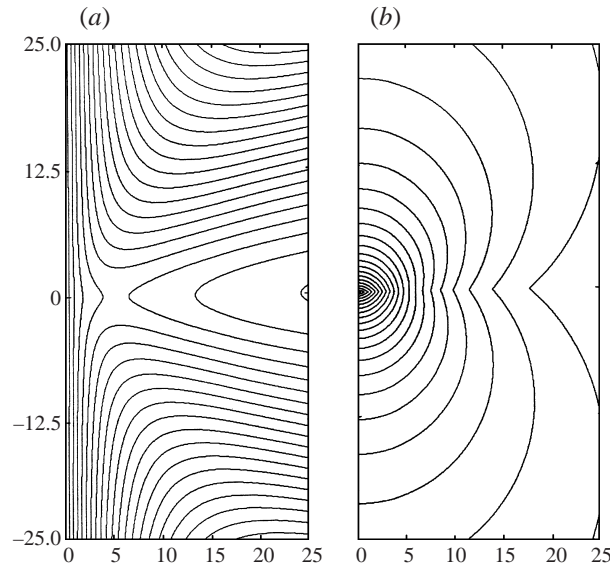
FIGURE 7. (*a*) The stream function and (*b*) the chemical potential for the asymptotic flow at a contact line. The asymptotic interface thickness is 0 in these units, because $\epsilon \to 0$ faster than $\sqrt{\mu \kappa}$. The interface is located at the $y = 0$ axis. Both the stream function and the chemical potential are symmetric about the interface. The wall is located at $x = 0$ and is moving downward with unit speed. Because the boundary condition is no-slip, the velocity right next to the wall must be the same as that of the wall. An inner no-slip boundary layer is clearly shown. This inner layer, in which the velocity points downward though the interface, extends out to about $x = 5.1$. Past this inner no-slip boundary layer, the velocity through the interface is always upward. The chemical potential obeys the jump condition (5.1) at the interface, hence the kinks in the contour lines there. The direction in which a kink points depends on the direction of the velocity there, to the right for downward flow, to the left for upward.

Because of the far-field condition that ψ equals 0 along the meniscus the asymptotic solution under consideration necessarily has no net through-flow. This seems to be the only reasonable condition for the unbounded case, because there are no far-field eigenfunctions with ψ not decaying to zero. However, the question arises as to whether this unbounded solution is applicable to flow between walls. As a test, numerical solutions have been found for the asymptotic equations (5.5), (5.6) for flow in a sidewall-driven square box. As in § 3 the box is half-filled by each fluid. The (asymptotically thin) interface runs horizontally at the box mid-height. The jump conditions (5.1)–(5.2) are applied at the interface. Because of symmetry, only the flow in the lower left-hand corner of the box needs calculation. Equations (5.5)–(5.8) were solved together with the no-flux, no slip boundary conditions at the bottom wall:

$$\psi = 0, \quad \frac{\partial \psi}{\partial y} = 0, \quad \frac{\partial \phi}{\partial y} = 0, \tag{6.7}$$

and the symmetry conditions at the vertical midline:

$$\frac{\partial \psi}{\partial x} = \frac{\partial^3 \psi}{\partial x^3} = \phi = 0. \tag{6.8}$$

Figure 8 shows the resulting flow in a 100×100 (in non-dimensional, microscale units) box. The square box results in a four-cell flow.

There are two contact lines in the cavity and, as is visible in figure 8, there can be
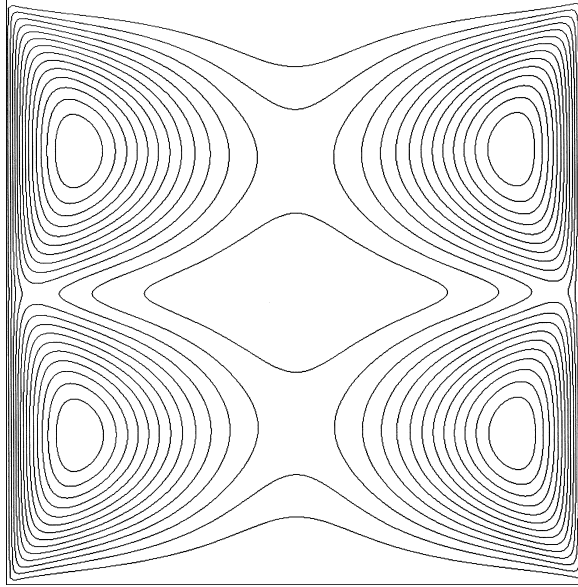
FIGURE 8. The stream function for the asymptotic flow in a 100×100 (in non-dimensional microscale units) box.

net downward flow at one and a compensating flow upward at the other. Three cavity sizes, 100×100, 200×200, and 400×400, were considered in an effort to estimate the net flow for each contact line as the cavity size approaches infinity. This net flow was found to be about 0.369 for the smallest box, about 0.233 for the middle box, and about 0.146 for the largest box. These fluxes are given by the absolute value of the stream function at the centre of the box. If the no-net-flux far-field solution is the relevant solution for understanding the box flow then these stream function values should become increasingly close to the stream function values of the unbounded solution. The stream function at large r for the unbounded flow is given to good accuracy by the $\psi_{F,2} + E_1\psi_1$ component of the far-field solution. $|\psi_{F,2} + E_1\psi_1|$ for the unbounded condition is 0.4466 for $\{r, \theta\} = \{50, 0\}$, 0.2611 for $\{100, 0\}$, and 0.1494 for $\{200, 0\}$. The flux between $r = 0$ and $r_{\text{boxcentre}}$ of the cavity solution thus appears to rapidly approach that of the no-net-flux unbounded solution as the cavity increases in size. As a corollary, the no-net-flow condition for the unbounded solution appears to be both relevant and correct.

7. The interface

This section discusses the solution to the C equation, equation (4.6). We determine the perturbation to interface location and interface slope, thus connecting the present theory to classical theory, and we also investigate the perturbation of the interface profile. We show that the equation for interface slope matches in form that of sharp-interface slip theory and that the perturbation to interface structure and to the energy of the interface is $O(\epsilon/\sqrt{\mu\kappa})$.

The C equation (4.6) and boundary condition (4.8) are non-dimensionalized by

$$x \to \sqrt{\mu\kappa}\, x, \quad y \to \epsilon y, \quad \phi \to \sqrt{\mu/\kappa}\, V_{\text{wall}}\, \phi. \tag{7.1}$$

The difference from the previous non-dimensionalization is that the y-direction is

stretched so that interface thickness becomes $O(1)$. Equations (4.6), (4.8) become

$$\alpha \frac{\partial^2 C}{\partial y^2} - \beta \Psi''(\bar{C})C + \alpha \left(\frac{\epsilon}{\sqrt{\mu\kappa}} \right)^2 \frac{\partial^2 C}{\partial x^2} = - \left(\frac{\epsilon}{\sqrt{\mu\kappa}} \right) Ca\, \phi, \tag{7.2}$$

$$\frac{\epsilon^2 \sigma \alpha D_w}{\sqrt{\mu\kappa}} \frac{\partial C}{\partial x} \bigg|_{x=0} = -\bar{C}_y V_{\text{wall}}, \tag{7.3}$$

where Ca is the capillary number. In these coordinates, equation (2.3b) becomes

$$\alpha \int \left(\frac{\partial C}{\partial y} \right)_{\text{eq}}^2 \mathrm{d}y = 1. \tag{7.4}$$

Since the non-dimensionalized ϕ is $O(1)$, (7.2) suggests that C is $O(\epsilon/\sqrt{\mu\kappa})$. This, however, is false. The left-hand side of (7.2) has an eigenfunction solution $C = \bar{C}_y$ and this produces a near-singularity that gives C an $O(\sqrt{\mu\kappa}/\epsilon)$ component. This component gives the deflection and slope of the perturbed interface. Higher-order terms then give the perturbation to the interface structure. The solution for C is of the form

$$C = -\frac{\sqrt{\mu\kappa}}{\epsilon} h(x)\bar{C}_y + \frac{\epsilon}{\sqrt{\mu\kappa}} \left(C_1 + \left(\frac{\epsilon}{\sqrt{\mu\kappa}} \right)^2 C_3 + \cdots \right). \tag{7.5}$$

The solution component $\bar{C}_y$ gives a unit downward translation of the meniscus without change of interface profile; $\sqrt{\mu\kappa}/\epsilon\, h(x)$ accordingly gives the perturbation to the height of the interface in the present stretched coordinates. The interface slope $\sqrt{\mu\kappa}/\epsilon\, \mathrm{d}h/\mathrm{d}x$ is $O(\sqrt{\mu\kappa}/\epsilon)$ because of the differently stretched x- and y-coordinates; $\mathrm{d}h/\mathrm{d}x$ by itself gives the slope as viewed in the original dimensional coordinates.

The equation for C_1 is

$$\alpha \frac{\mathrm{d}^2 C_1}{\mathrm{d}y^2} - \beta \Psi''(\bar{C})C_1 = \left(\alpha \bar{C}_y \frac{\mathrm{d}^2 h}{\mathrm{d}x^2} - Ca\, \phi \right). \tag{7.6}$$

The left-hand side of (7.6) has the homogenous solutions $\bar{C}_y$ and $\bar{C}_y \int_0^y (1/\bar{C}_y^2)\,\mathrm{d}y$. The first is even, bounded at ∞, and an eigenfunction. The second is odd and unbounded at ∞. Because of the eigenfunction, for a solution to exist the integral $\int_0^\infty \bar{C}_y (\alpha \bar{C}_y (\mathrm{d}^2 h/\mathrm{d}x^2) - Ca\phi)\,\mathrm{d}y$ must equal zero. Using (7.4) and the fact that ϕ is very slowly varying in y, this constraint leads to

$$\frac{\mathrm{d}^2 h}{\mathrm{d}x^2} = Ca\, \phi(x, 0). \tag{7.7}$$

The wall boundary condition for h, found by substituting $C = -(\sqrt{\mu\kappa}/\epsilon)h(x)\bar{C}_y$ into (7.3), is

$$\epsilon \sigma \alpha D_w \frac{\mathrm{d}h}{\mathrm{d}x} \bigg|_{x=0} = V_{\text{wall}}. \tag{7.8}$$

The far-field solution for the meniscus slope is found by substituting (6.5) into (7.7). The result, to lowest order, is

$$h_x = \frac{V_{\text{wall}}}{\epsilon \sigma \alpha D_w} + Ca\, (4A \ln r + \text{const.}) \tag{7.9}$$

where the constant must be determined from the inner solution. In dimensional

coordinates (7.9) becomes

$$h_x = \frac{V_{\text{wall}}}{\epsilon\sigma\alpha D_w} + Ca\left(4A\ln r - 4A\ln\sqrt{\mu\kappa} + \text{const.}\right) \tag{7.10}$$

This is the same form as deduced by Cox (1986) for his two-region analysis. As discussed in §2, D_w is taken in this analysis to be at least $O(1/\epsilon)$. $V_{\text{wall}}/\epsilon\sigma\alpha D_w$ is thus $O(Ca)$ or smaller. The dimensional form of Cox's equation (5.4) (Cox 1986, p. 178) is equivalent to

$$h_x = Ca\left(f(\pi/2,1)\ln r - f(\pi/2,1)\ln s + \text{const.}\right). \tag{7.11}$$

In (7.11) the slip length s replaces $\sqrt{\mu\kappa}$ in equation (7.10). Cox's stress function $f(\theta_{\text{eq}},\lambda)$ evaluated for $\theta_{\text{eq}} = \pi/2$ and a viscosity ratio of 1 replaces (and equals) $4A$. Cox assumes that the microscopic contact angle is the same as the equilibrium angle, which is equivalent to setting D_w equal to ∞.

The constant in (7.9), (7.10) is determined from the $\{\psi,\phi\}$ near-field solution. From this and equation (7.8) the undetermined constant is found to be about 0.643:

$$h_x \simeq \frac{V_{\text{wall}}}{\epsilon\sigma\alpha D_w} + Ca\left(4A\ln\frac{r}{\sqrt{\mu\kappa}} + 0.643\right). \tag{7.12}$$

An equation relating h to the pressure field can also be derived. The linearization of (2.9) gives

$$\mu\nabla^2 u = \frac{\partial p}{\partial x} - \epsilon\sigma\alpha\bar{C}_y\frac{\partial^2 C}{\partial y\partial x} + \epsilon\sigma\alpha\bar{C}_{yy}\frac{\partial C}{\partial x}, \tag{7.13}$$

$$\mu\nabla^2 v = \frac{\partial p}{\partial y} + \epsilon\sigma\alpha\bar{C}_y\frac{\partial^2 C}{\partial x^2}. \tag{7.14}$$

These are in dimensional form. Integration of (7.14) through the interface yields

$$\epsilon\sigma\alpha\frac{\mathrm{d}^2}{\mathrm{d}x^2}\int \bar{C}_y C\,\mathrm{d}y = -(p_+ - p_-). \tag{7.15}$$

Since $u_+ = u_-$ and, from the continuity equation, $\partial u/\partial x|_{0_+} = \partial u/\partial x|_{0_-}$ implies $\partial v/\partial y|_{0_+} = \partial v/\partial y|_{0_-}$, and since $\mu_+ = \mu_-$, the viscous terms drop out. The same integration/reduction procedure as used to derive (7.7) then gives

$$\sigma\frac{\mathrm{d}^2 h}{\mathrm{d}x^2} = p_+ - p_-. \tag{7.16}$$

Since p is antisymmetric, this can be rewritten:

$$\sigma\frac{\mathrm{d}^2 h}{\mathrm{d}x^2} = -2p_-. \tag{7.17}$$

With the scalings $x \to \sqrt{\mu\kappa}\,x$, $h \to \sqrt{\mu\kappa}\,h$, $p \to \frac{1}{2}\mu V_{\text{wall}}/\sqrt{\mu\kappa}\,p$, (7.17) becomes

$$\frac{\mathrm{d}^2 h}{\mathrm{d}x^2} = -Ca\,p_-. \tag{7.18}$$

Thus along the interface, $p_+ = -p_- = \phi$.

We return briefly to C_1. From (7.7), equation (7.6) becomes

$$\alpha\frac{\mathrm{d}^2 C_1}{\mathrm{d}y^2} - \beta\Psi''(\bar{C})C_1 = Ca\left(\alpha\bar{C}_y\phi(x,0) - \phi\right). \tag{7.19}$$

Since the two homogenous solutions are known the complete solution can be

written down using the method of variation of parameters. C_1 gives the leading-order perturbation to the meniscus profile. The solution is non-singular and behaves like $Ca\ \phi/\beta\Psi''(\bar{C})$ as $y \to \infty$. The perturbation to interface structure is uniformly $O(Ca\,\epsilon/\sqrt{\mu\kappa})$. The leading-order perturbation to the surface tension is $2\alpha\sigma \int \bar{C}_y C_{1,y}\,\mathrm{d}y$, in non-dimensional coordinates. This is also $O(Ca\ \epsilon/\sqrt{\mu\kappa})$.

8. The case $\epsilon/\sqrt{\mu\kappa} = O(1)$

The case $\delta = 2$, $\epsilon/\sqrt{\mu\kappa} = O(1)$ has the same two-region solution structure as $\delta < 2$, $\epsilon/\sqrt{\mu\kappa} \to 0$. The far-field solution is the same for both cases. The near-field solution is different because for $\delta = 2$ the details of the solution become dependent on the shape of the interface profile.

We look first at the solution for the potential and velocity field. The far-field solution and solution structure, equations (6.1)–(6.6), remains valid. With $O(\sqrt{\mu\kappa}) = O(\epsilon)$ there is no longer a definite outer scale so it can be useful to write these equations dimensionally. In particular, the dimensional chemical potential is

$$\phi_{F,0,\mathrm{dim}} = \mu V_{\mathrm{wall}} \left(-\frac{8}{\pi} A \frac{\ln\left(r/\sqrt{\mu\kappa}\right)}{r} \sin\theta + \frac{4A}{r} \left(\frac{2}{\pi}\theta\cos\theta + \cos\theta \right) \right). \tag{8.1}$$

The magnitude of the chemical potential is proportional to the viscous forcing μV_{wall}. There is a weak dependence on the diffusive length scale $\sqrt{\mu\kappa}$ through the equation's log term. Equation (8.1) is valid for $r \gg \epsilon$. In the $r = O(\epsilon) = O(\sqrt{\mu\kappa})$ region a numerical solution must be carried out that includes the details of the interface structure. The solution is the same in character and is carried out using the same method as for the $\epsilon/\sqrt{\mu\kappa} \to 0$ case.

When $\epsilon/\sqrt{\mu\kappa}$ is $O(1)$, ϕ in the inner region can no longer be considered to be slowly varying on the $O(\epsilon)$ length scale. The asymptotic expansion given by (7.5) is therefore no longer useful in the inner region but it continues to be valid in the far field. The local rate of convergence of the expansion is approximately ϵ/r. From (7.2), the perturbation to C in the near field is $O(Ca\,\epsilon/\sqrt{\mu\kappa})$. Equation (7.10) for h_x therefore remains valid but with its constant now being a function of the interface profile.

9. Non-90° contact angles

This section discusses some results for non-zero $g(C)$. Results are primarily computational. Their main purpose is to show the reader that the chief results from the previous sections, in particular the ability of a diffuse interface contact line to stop most through-flow and the increasing integrity of the interface as it becomes thinner, carry over to the non-90° case.

First, however, an important fact that must be pointed out is that the wall free energy $\gamma g(C)$ (see equation (2.13)) is not in general the same as the total wetting energy. With non-zero $g(C)$, layers are formed on walls that, in equilibrium, obey

$$\epsilon\sigma\alpha\frac{\mathrm{d}^2\bar{C}}{\mathrm{d}x^2} - \epsilon^{-1}\sigma\beta\Psi'(\bar{C}) = 0 \tag{9.1}$$

with the boundary conditions

$$\epsilon\sigma\alpha\frac{\partial\bar{C}}{\partial x} + \gamma g'(\bar{C}) = 0 \quad \text{at } x = 0, \quad \bar{C} = C_{\mathrm{bulkphase}} \quad \text{at } x = \infty. \tag{9.2}$$

This minimizes the total of the layer energy plus the wall energy, which is the total wetting energy. The layer – relative to the bulk phase at $x = \infty$ – is enriched with one of the fluids, depleted in the other. These effects can be of very great interest, see for example de Gennes' (1985) discussion of critical wetting. However, we do not want yet to consider such complicating effects. The wall free energy and the total energy become the same and the wall layer disappears when $g'(C_{\text{bulkphase}}) = 0$. The calculations shown here are for only this simpler, but still important, situation.

With this limitation, the most significant differences between the 90° and non-90° degree cases are (i) a change in far-field eigenfunction structure and a resulting change in the far-field behaviour of the chemical potential and (ii) a change in the structure of the mathematical representation of the far-field solution. Equations (5.5)–(5.7) continue to be valid. The jump conditions (5.1), (5.2) at the interface become

$$\frac{1}{r}\frac{\partial \phi}{\partial \theta}\bigg|_{+} - \frac{1}{r}\frac{\partial \phi}{\partial \theta}\bigg|_{-} = \frac{\partial \psi}{\partial r} \tag{9.3}$$

and

$$\frac{1}{r^3}\frac{\partial^3 \psi}{\partial \theta^3}\bigg|_{+} - \frac{1}{r^3}\frac{\partial^3 \psi}{\partial \theta^3}\bigg|_{-} = -\frac{\partial \phi}{\partial r}. \tag{9.4}$$

We use the same r, θ coordinates as in §6. The θ at which these conditions are applied is designated θ_c, where θ_c is equal to the equilibrium wedge angle of the advancing fluid minus $\pi/2$. The system is no longer symmetric so the entire domain $x \geqslant 0$ must be considered. The quantities ψ, $\partial \psi/\partial \theta$, $\partial^2 \psi/\partial \theta^2$, and ϕ are continuous at the interface.

As with the 90°($\theta_c = 0$) case the far-field solution can be represented in terms of a forced solution plus an infinite set of far-field eigenmodes. The stream function component of the forced solution is, again, the wedge flow solution of Huh & Scriven (1971). The resulting forced chemical potential is of the form

$$\Psi_F \simeq \frac{1}{r}\sin\theta / \sin\theta_c. \tag{9.5}$$

This solution form fails for $\theta_c = 0$, i.e. for the 90° contact angle case already considered. Unlike for the solution for $\theta_c = 0$ there is no cascade to higher-order terms. This is because Ψ_F is analytic: there is no jump in its derivative at the interface. The far-field eigenfunctions divide into two subsets. In the first set the leading-order term of the chemical potential is identically zero in the advancing fluid and of the form

$$\frac{1}{r^{\xi_n}}\sin\xi_n(\theta - \theta_c), \qquad \xi_n = n\frac{\frac{1}{2}\pi}{\frac{1}{2}\pi - \theta_c}, \quad n = 1, 3, 5, \ldots . \tag{9.6}$$

in the receding; ξ_n is chosen so that boundary conditions

$$\phi(\theta_c) = 0, \qquad \frac{\partial \phi}{\partial \theta}\bigg|_{\pi/2} = 0 \tag{9.7}$$

are satisfied. The stream function eigenfunction is forced by the jump condition (9.3). It also behaves like $1/r^{\xi_n}$. The chemical potential eigenfunctions in the second set are zero in the receding fluid, behave like (9.6) in the advancing, and have $\xi_n = n\pi/2/(\pi/2 + \theta_c)$, $n = 1, 3, 5, \ldots$. In general, the leading-order potential behaves very differently in the two fluids. For $\theta_c = -\pi/4$ its receding fluid behaviour is like $r^{-2/3}$. In the advancing fluid its far-field behaviour is dominated by ϕ_F. The leading-order eigenfunction there behaves like r^{-2}. As θ_c approaches 0, the forced mode and
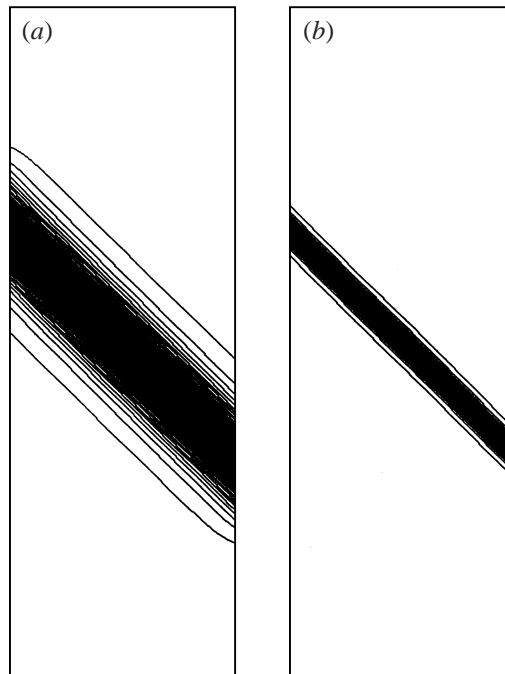
FIGURE 9. Equilibrium (motionless) thick and thin interfaces. The left-hand wall is preferentially wetted by the lower fluid, the right-hand wall by the upper. $g(C)$ is $+15\sqrt{2}(3C - 4C^3)/2$ for the left-hand wall, the opposite for the right. The interfaces are at the expected 45° angle.

the leading-order receding fluid and advancing fluid eigenfunctions merge to give the $\ln r/r$ behaviour found in §6.

The calculations of §3 have been repeated for the case of a 45° contact angle ($\theta_c = -45°$). All parameters are the same as in that section except for the addition of $g(C) = \pm15\sqrt{2}(3C - 4C^3)/2$. C varies from $-1/2$ to $+1/2$ so the jump in wall energy from the relatively wetting fluid to the other is $30/\sqrt{2}\,\mathrm{erg\,cm}^{-2}$. Since the surface tension is 30 dynes/cm the indicated equilibrium contact angle is 45°. Figure 9 shows two diffuse interfaces, one thick, one thin, in their equilibrium state. Their thicknesses are the same as the thick and thin interfaces in §3. The sidewalls have been assigned opposite $g(C)$ – one is preferentially wet by the lower fluid, the other by the upper. The result is a straight meniscus running from one sidewall to the other. This allows the interface slope and perturbations to it to be easily measured. Figure 10 shows the same interfaces at $Ca = 0.01333$. Each suffers about the same perturbation to its average slope. As in §3 we see that the thinner interface suffers much less structural perturbation. Figure 11 shows the chemical potential for the thick interface. It is qualitatively in agreement with analysis; the potential decays much more rapidly in the wetting fluid (because of its narrower wedge at the contact line) than in the non-wetting.

Figures 10 and 11 show results for a wetting flow, i.e. the more wetting fluid is advancing. The analysis in this paper is linear so it does not distinguish between wetting and dewetting. Preliminary calculations have been made for this fluid system for dewetting flow. These show a very different behaviour than for wetting. The calculations show complete contact line failure at a Ca of about -0.008 and a transition to film formation (a residue of the more wetting fluid left on and near
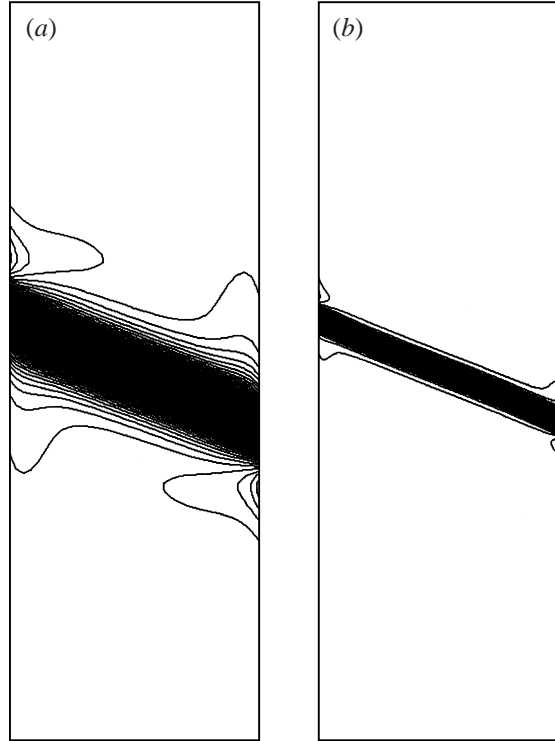
FIGURE 10. Same as figure 9 but with the left wall moving down, the right wall up. $Ca = 0.01333$.
The macroscopic slope is changed but the interface slope right at the walls remains 45°.

the receding wall) at about $Ca = -0.006$. For dewetting, linear theory appears to be
accurate down to a Ca of only about -0.003.

Calculations have also been made for a 30° contact angle. These give a transition
to film flow at about $Ca = -0.003$.

10. Comparison of numerical calculations to theory

This section looks at the nonlinear numerical calculations of §3 and compares
them to the theoretical results of §6 and §7 and the linear box calculations of §6.
The calculations in §3 have interfaces with very large thicknesses. Related to that,
their ratio $\epsilon/\sqrt{\mu\kappa}$ is large, contrary to the regime dealt with by the theory. Can their
results nevertheless be related to the asymptotic theory? We show here that these 'fat
interface' results appear to approach those of asymptotic theory according to $O(\epsilon^2)$.

According to (7.12) if κ is halved then the slope of an interface with a moving
contact line increases by $2Ca\,A \ln 2$. For the calculations in §3, with $Ca = 0.01333$,
this equals about 0.0198. These calculations are for a μ of 1. For the thick meniscus
κ is 2.65×10^{-5} cm^5 s^{-1} erg^{-1} and for the thin meniscus it is 6.625×10^{-6}. In non-
dimensional units the driven cavity has a size of 388.3 by 1164.9 for the thick meniscus,
twice that for the thin; $\epsilon/\sqrt{\mu\kappa}$ for the thin meniscusis is about 62.9.

For these parameters, equation (7.12) with r set equal to 1 (the left-to-right midline
of the box) gives an h_x for the thick meniscus calculation of about 0.309. For the thin
meniscus (7.12) gives 0.348. The numerical calculations in §3 give, respectively, 0.331
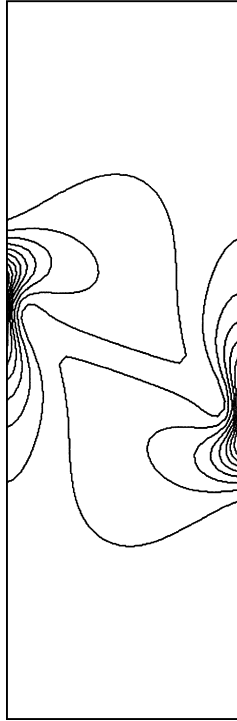
FIGURE 11. The chemical potential for the thick meniscus of figure 10. The potential decays much more rapidly in the wetting fluid (because of its narrower wedge against the wall) than in the non-wetting.

and 0.336. The numerical results are qualitatively right, but the expected increase in slope with increasing container size is lacking.

Relating the calculations in § 3 to the asymptotic theory involves two adjustments. The first is for the finite thickness of the interfaces, the second is for the effects of the box enclosure. To judge the first effect the calculations in § 3 have been redone with interfaces with different thicknesses. Halving the interface thickness for the 388.3 × 1164.9 calculation results in a slope of 0.283; halving it again yields 0.268. Halving the interface thickness for the 776.6 × 2329.8 enclosure yields a slope of 0.314 while doubling it gives 0.377. Extrapolating these results using a second-order extrapolation yields $\epsilon = 0$ slopes of 0.259 for the small container and 0.292 for the large. Extrapolating using a third-order approximation and assuming an $O(\epsilon^2)$ dependence of the slope as $\epsilon \to 0$ yields 0.262 and 0.304. These adjusted results, particularly those for the second extrapolation, demonstrate close to the same increase in slope with increase in domain size that is predicted by theory. However, the difference of these results from the asymptotic theory has now increased.

This difference is accounted for by effects of the top and bottom walls of the box enclosure. A calculation using the asymptotic theory (equations (5.5)–(5.6) with the jump conditions (5.1)–(5.2) has been made for the smaller enclosure. This yields a midpoint slope of 0.260, in good agreement with the extrapolations. An asymptotic calculation for the larger enclosure is, unfortunately, too expensive. However, to further study enclosure effects nonlinear calculations have also been made for the box enclosure discussed in § 6. The linearized box calculations of § 6 yield midpoint slopes of 0.143 for the 100 × 100 box, 0.182 for the 200 × 200 box, and 0.222 for the

400×400 box. h_x increases at almost exactly the same rate as given by the asymptotic result for the single contact line but the square box enclosure changes the slope from that of the semi-infinite interface by a constant roughly equal to 0.08. Nonlinear calculations made for the 400×400 box for the three different interface widths of § 3 give a midpoint h_x for the thickest interface of 0.284, for the middle, 0.238, and for the thinnest, 0.225. The convergence towards the result of the asymptotic linearized calculation appears to be $O(\epsilon^2)$.

Another measure of the distance/closeness of macroscopic interface and asymptotic results is found in the potential field. Since the spatial non-dimensionalization is isotropic the potential field in the asymptotic and § 3 calculations should have the same appearance. Comparing figure 6 to figure 7(*b*), we see that the outer regions of the two fields match well – the logarithmic term in equation (6.5) explains the necking down at the meniscus. Right at the contact line, however, the two are in disagreement. The asymptotic result shows the potential gradient oriented roughly parallel to the wall while the results in § 3 show it perpendicular. Again, this disagreement seems to be due to differences in meniscus width. Another easy point of comparison is the potential maximum, which occurs right at the contact line. The calculations are in agreement with theory in that the maximum potential is very close to inversely proportional to the square root of the mobility. The coarse meniscus calculation has a maximum potential 59% of that predicted by the asymptotic theory, the fine calculation increases to 66%. Some additional linearized calculations have been made that indicate continuing slow increase in this ratio with increasingly thin menisci.

11. Nanoscale calculations

The results so far have not addressed the question of whether or not realistic diffusivities and levels of interdiffusion could possibly play a role in regularizing moving contact lines. In this section we look at results from direct simulations of realistically scaled interfaces with realistic liquid–liquid diffusivities. Liquid–liquid interfaces away from critical points are about $1\,\mathrm{nm}$ thick ($10^{-7}\,\mathrm{cm}$), about three or four molecular lengths. A typical molecular diffusion rate is about $10^{-5}\,\mathrm{cm}^2\,\mathrm{s}^{-1}$. The macroscopic interface calculations presented in § 3 had interface thicknesses about 10^6 larger than realistic and a diffusivity about 10^3 too large.

The calculations presented in this section are for the same geometry, wall velocities, surface tension, and viscosity as in § 3, but with the cavity size drastically scaled down. Most calculations are of a $16 \times 48\,\mathrm{nm}$ cavity but some have been made at twice and four times that, in order to investigate the domain-size dependence of the results. The calculations are at about four to sixteen times the scale of moving contact line molecular dynamics calculations by Koplik *et al.* (1989) and Thompson & Robbins (1989). As in § 3, $\Psi(C)$ is modelled as $(C - 1/2)^2(C + 1/2)^2$. Its α, β and tanh equilibrium profile and a definition of its interface thickness are given in § 3. Its relationship between diffusivity and mobility is $D = \epsilon^{-1}\sigma\beta\kappa\Psi''(C_{\mathrm{bulkphase}}) = 24\tanh^{-1}(0.9)\epsilon^{-1}\sigma\kappa \simeq 35.33\epsilon^{-1}\sigma\kappa$.

Diffuse-interface Stokes flow is invariant to a transformation that can be used to connect the calculations of § 3 to nanoscale calculations. If the domain of flow is shrunk or expanded by a given factor, if ϵ is changed by the same factor, and if the mobility is changed by the factor squared, viscosities, surface tension, densities, and velocity boundary conditions remaining the same, then steady-state flow fields and interface positions are the same at each scale. The thin interface calculation in § 3 has an ϵ of about $0.16\,\mathrm{cm}$ and a mobility of 6.6×10^{-6}. The corresponding

thickness and mobility in a 16 by 48 nm box (scale factor 8×10^{-7}) are 1.29 nm and 4.2×10^{-18}. The diffusivity in the calculations in §3 is about 0.043 cm^2 s^{-1}. In the rescaling the diffusivity is changed by the scale factor and it becomes about 3.5×10^{-8}. The calculations in §3 are at finite Reynolds number ($Re = 0.8$) so the transformation in this case does not hold perfectly. Still, considering the low interfacial distortion shown in the thin interface results of §3 and the extremely low diffusivity at realistic interface widths that those calculations correspond to, it appears that diffusion is definitely a candidate for being a mechanism for contact line regularization.

Nanoscale calculations have been carried out for a wide range of diffusivity and slip. The slip model used was

$$(v - V_{\text{wall}}) = -S\mu \frac{\partial v}{\partial x_n} = -L \frac{\partial v}{\partial x_n} \tag{11.1}$$

where x_n is the direction into the wall and $\mu \partial v / \partial x_n$ is the wall shear stress. L is the inner scale or slip length that would be set by shear in the absence of chemical potential effects. The interface thickness was set to 1.2 nm. With no slip, and under these conditions, it was found that diffusion can maintain the interface profile with no noticeable perturbation down to about $D = 10^{-7}$. At $D = 10^{-8}$ the contact line is maintained but the interface profile is distorted. The chemical potential loses its characteristic half-dumbbell shape and begins to align itself parallel to the convectively thickened/thinned interface. At $D = 10^{-9}$ the contact line begins to fail. With $D = 10^{-5}$ the mobility is about 1.1×10^{-15}†, giving a diffusive length scale of about 3.3×10^{-8}. In agreement with the analysis, the inner no-slip velocity layer has a width of about 1.4 nm.

The effects of slip were investigated for $D = 10^{-6}$. At $S = 10^{-6}$ ($\mu = 1$ P, so $L = S$ in all the following calculations) the maximum velocity reached in the 16 by 48 box is only 0.12 cm s^{-1} ($V_{\text{wall}} = 0.4$). Slip effects are dominant and extend the whole length of the enclosure. For the no-slip case, the maximum chemical potential for $D = 10^{-6}$ is 4.7×10^7 erg cm^{-3}. This corresponds to a local dissolution of one phase in the other of about 1%. The maximum chemical potential force on the fluid is about 5×10^{14} erg cm^{-4}. With $S = 10^{-6}$ the chemical potential keeps its half-dumbbell shape but is greatly reduced in amplitude, to a maximum of about 3.2×10^6. Diffusive fluxes are therefore only about one fourteenth that of the no-slip case. With $S = 10^{-7}$, slip and diffusion are competitive in effect. The maximum velocity is 0.34 and the maximum chemical potential is 1.7×10^7. With $S = 10^{-8}$ diffusion effects are dominant. The maximum chemical potential is about 85% that of the no-slip case.

The no-slip $D = 10^{-6}$ case was also calculated for the 48 by 144 nm box. The average slope of the interface in the large box is 0.253. In the small box it is 0.144, for a difference of 0.109. (The theoretical difference, from equation (7.12) for $r \to \infty$, is 0.079.) Except for this, there is little change from one calculation to the other. The maximum chemical potential in the large box is 2% greater than in the small. The no-slip inner velocity layer is in each case about 5 Å. The minimum radius of curvature of the interface, found at the contact line, is in both cases about 10 nm.

The above calculations have been rather conservative in that they have considered both small diffusivities and large slip lengths. The molecular dynamics calculations of Koplik *et al.* and Thompson & Robbins indicate slip lengths of at most about 3 Å. The yield-stress analysis of Durbin (see §3) gives close to the same result. Barrat

---

† This mobility is an order of magnitude below generally accepted values. $D = 10^{-5}$ is typical for ideal solutions but may be low for non-ideal diffusion near interfaces.

& Bocquet also agree, provided that the fluids involved each individually partially wet the wall. $L = 10^{-6}$ therefore seems to be completely unrealistic. From Barrat & Bocquet, $L = 10^{-7}$ appears to be close to the upper limit for slip length for fluid systems with fluid–vapour contact angles less than 100°. The implication of the calculations in this section is therefore that chemical potential effects are competitive with and perhaps dominant over shear-induced slip.

12. Conclusions

The CHW interface model is a very approximate but nevertheless widely used fluid interface model. Though it has generally been used in the context of diffusion processes there has been an increasing interest in the condensed matter, critical fluids, and computational fluid dynamics communities in using it for fluid dynamics modelling.

This work was begun to find out if the CHW model could validly and usefully be used for contact line flows. This question can be looked at from either a macroscopic or microscopic point of view.

The macroscopic results are that the CHW contact line has the same far-field behaviour as the more traditional sharp-interface slip models of contact line flow. A computational fluid dynamicist interested in only macroscopic results can thus use either model. Certain difficult to know parameters enter into both: in the case of slip models it is the material-dependent slip length, in the case of the CHW model it is the material-dependent mobility κ. If κ or the slip length are unknown the accuracy of the results will be only qualitative unless some empirical matching is made to experiments. Fortunately, the sensitivity of the macroscopic contact angle to these unknowns, being logarithmic, is unlikely to be ruinous.

The microscopic results have shown that chemical potential effects may be dominant over shear and that it may be possible for a moving contact line to be regularized even with no-slip boundaries. We have looked at the case of regularization achieved via chemical diffusion driven by intermolecular potential gradients. Chemical potential induced compressibility (Seppecher 1996) probably also plays an important role. The diffusion model used in this paper is the standard model introduced by Cahn. The results herein have been derived for general bulk free energy $\Psi(C)$. They therefore apply both to near-critical fluid mixtures and to mixtures far from critical for which deep-quench or double-obstacle free energy models would be appropriate. The applicability of the CHW model to realistically thick interfaces with realistic mobilities has been shown by the nanoscale calculations in § 11. A difficulty is that the diffusion length scale can be very small, indicating that subcontinuum effects may have to be carefully modelled.

A related question is which model of contact line regularization – shear-slip or chemical-potential driven fluxes – is likely to further our understanding of contact line flow? It seems worthwhile to look at CHW dewetting and try to determine if it matches to experiments. The preliminary results reported in § 9 show that CHW dewetting is very different from wetting and that the CHW model gives a dewetting failure at very low capillary number. Another flow problem that could be looked at is the instability of a thin film lying on a solid. Unlike one-dimensional lubrication models, Navier–Stokes/CHW calculations of its evolution could be followed to complete rupture – the appearance of a contact line – and beyond. The Navier–Stokes/CHW model would be more difficult to solve than a one-dimensional lubrication model, but much easier than models that rely on two-dimensional mean-field integrals of

molecular attractions (see Indeikina & Chang 1998). A third problem that the CHW model could be useful for is the fluid dynamics involved in phase nucleation against solids.

This paper has not argued that the CHW model is in detail correct. In fact, it has been known almost since its inception that a basic assumption underlying it – that fluid interfaces are thick enough so that composition gradients across them can be validly time-averaged and then differentiated – is, except perhaps for near-critical fluids, not true. Given the large diffusive fluxes, the simple diffusion model that this paper has used is also only qualitatively correct. It is hoped that, nevertheless, the CHW model points toward the right physics, which are very basic: (i) that the contact line kinematic and stress singularities can be resolved by the two phases having differing directions of flux; (ii) that the contact line composition profile at the wall can be maintained by the diffusive interchange of particles; and (iii) that bond breaking at the wall is caused by chemical potential forces.

Appendix. Linearized version of Seppecher's analysis

The following may help the interested reader compare Seppecher's work to the work in this paper. Seppecher discusses a model compressible Cahn–Hilliard fluid that is isothermal, has the free energy density

$$f = \tfrac{1}{2}\epsilon\sigma\alpha|\nabla\rho|^2 + \epsilon^{-1}\sigma\beta\Psi(\rho) \qquad (A\,1)$$

and has no separate p–V–T relationship, so that the fluid's thermodynamics is completely described by (A 1). The equations of motion for this fluid are

$$\rho\frac{\mathrm{D}u_i}{\mathrm{D}t} = \nabla\cdot\tau_{\mathrm{visc},i} - \rho\nabla\phi, \qquad (A\,2)$$

$$\frac{\partial\rho}{\partial t} = -\sum_i\frac{\partial\rho u_i}{\partial x_i}. \qquad (A\,3)$$

The steady, dynamic contact line equations linearized about a 90° equilibrium contact angle are

$$\nabla\cdot\tau_{\mathrm{linvisc},i} = \bar{\rho}\nabla\phi, \qquad (A\,4)$$

$$\sum_i\frac{\partial\bar{\rho}u_i}{\partial x_i} = 0. \qquad (A\,5)$$

Outside the $O(\epsilon)$ thick interface, these equations are incompressible:

$$\bar{\mu}_\pm\nabla^2 u = \bar{\rho}_\pm\frac{\partial\phi}{\partial x}, \qquad (A\,6)$$

$$\bar{\mu}_\pm\nabla^2 v = \bar{\rho}_\pm\frac{\partial\phi}{\partial y}, \qquad (A\,7)$$

$$\frac{\partial u}{\partial x} + \frac{\partial v}{\partial y} = 0; \qquad (A\,8)$$

$\bar{\mu}$ and $\bar{\rho}$ take on different constant values above and below the interface. In these regions $\bar{\rho}\phi$ is the same, to within a constant, as the pressure.

Away from the contact line (A 4) can be integrated through the interface to yield

$$\bar{\mu}_+\left(\frac{\partial u}{\partial y}+\frac{\partial v}{\partial x}\right)\Big|_{0_+}=\bar{\mu}_-\left(\frac{\partial u}{\partial y}+\frac{\partial v}{\partial x}\right)\Big|_{0_-}, \tag{A 9}$$

$$2\bar{\mu}_+\frac{\partial v}{\partial y}\Big|_{0_+}-2\bar{\mu}_-\frac{\partial v}{\partial y}\Big|_{0_-}=\bar{\rho}_+\phi(x,0_+)-\bar{\rho}_-\phi(x,0_-)-\int\bar{\rho}_y\phi(x,y)\,\mathrm{d}y. \tag{A 10}$$

Equation (A 9) plus the conditions $u_+=u_-$ and $v_+=v_-=0$ are used as boundary conditions to find the far-field hydrodynamic solution. This is the same solution as given by Cox (1986). In the case of $\mu_-=\mu_+$, which was the case considered by Seppecher, the far-field solution is given by (6.3). A far-field potential is forced by the hydrodynamic solution through (A 6)–(A 8).

The meniscus equation is found by the same integration/reduction as in §7. The linearized relationship between density and the chemical potential is

$$\epsilon\sigma\alpha\nabla^2\rho-\epsilon^{-1}\sigma\beta\Psi''(\bar{\rho})\rho=-\phi. \tag{A 11}$$

The integration/reduction procedure yields

$$\sigma\frac{\mathrm{d}^2h}{\mathrm{d}x^2}=\int\bar{\rho}_y\phi(x,y)\,\mathrm{d}y \tag{A 12}$$

which, from (A 10), becomes

$$\sigma\frac{\mathrm{d}^2h}{\mathrm{d}x^2}=\bar{\rho}_+\phi(x,0_+)-\bar{\rho}_-\phi(x,0_-)-\left(2\bar{\mu}_+\frac{\partial v}{\partial y}\Big|_{0_+}-2\bar{\mu}_-\frac{\partial v}{\partial y}\Big|_{0_-}\right). \tag{A 13}$$

The meniscus profile forced by the far-field flow is of the usual form:

$$h_x=Ca(4A^*\ln r+\text{const.}); \tag{A 14}$$

A^* is the variable viscosity generalization of the coefficient A given by (6.1b).

Near the contact line, the contradiction between the far-field solution ($v_-=v_+=0$) and the flow at the wall ($v_-=v_+=V_{\text{wall}}$) is resolved in an $O(\epsilon)$-scale near field. There the full equations (A 4) and (A 5) must be solved, with the far-field solution used as the $r\to\infty$ boundary condition. The near-field solution determines the constant in (A 14). Like the $\epsilon/\sqrt{\mu\kappa}=O(1)$ case discussed in §8, this constant depends on the details of the meniscus profile, in other words, on the choice of Ψ.

REFERENCES

ANDERSON, D. M. & MCFADDEN, G. B. 1997 A diffuse-interface description of internal waves in a near-critical fluid. *Phys. Fluids* **9**, 1870–1879.

ANDERSON, D. M., MCFADDEN, G. B. & WHEELER, A. A. 1998 Diffuse-interface methods in fluid mechanics. *Ann. Rev. Fluid Mech.* **30**, 139–165.

ANTANOVSKII, L. K. 1995 A phase field model of capillarity. *Phys. Fluids* **7**, 747–753.

BARRAT, J.-L. & BOCQUET, L. 1999 Large slip effects at a nonwetting fluid–solid interface. *Phys. Rev. Lett.* **82**, 4671–4674.

BATES, P. W. & FIFE, P. C. 1993 The dynamics of nucleation for the Cahn–Hilliard equation. *SIAM J. Appl. Maths* **53**, 990–1008.

BLAKE, T. D. 1993 Dynamic contact angles and wetting kinetics. In *Wettability* (ed. J. C. Berg), pp. 251–309. Marcel Dekker.

BRACKBILL, J., KOTHE, D. B. & ZEMACH, C. 1992 A continuum method for modeling surface tension. *J. Comput. Phys.* **100**, 335–354.

CAHN, J. W. 1961 On spinodal decomposition. *Acta Metallurgica* **9**, 795–801.

CHELLA, R. & VIÑALS, J. 1996 Mixing of a two-phase fluid by cavity flow. *Phys. Rev.* E **53**, 3832–3840.

COX, R. G. 1986 The dynamics of the spreading of liquids on a solid surface. Part 1. Viscous flow. *J. Fluid Mech.* **168**, 169–194.

DURBIN, P. 1988 Considerations on the moving contact-line singularity, with application to frictional drag on a slender drop. *J. Fluid Mech.* **197**, 157–169.

DUSSAN V., E. B., RAME E. & GAROFF, S. 1991 On identifying the appropriate boundary conditions at a moving contact line: an experimental investigation. *J. Fluid Mech.* **230**, 97–116.

GENNES, P. G. DE 1985 Wetting: statics and dynamics. *Rev. Mod. Phys.* **57**, 827–863.

GENNES, P. G. DE, HUA, X. & LEVINSON, P. 1990 Dynamics of wetting: local contact angles. *J. Fluid Mech.* **212**, 55–63.

GIBBS, J. W. 1878 On the equilibrium of heterogenous substances. *Trans. Conn. Acad.* **3**, 108–248, 343–524. Reprinted in *The Scientific Papers of J. Willard Gibbs*, pp. 55–371. Oxbow Press.

GURTIN, M. E., POLIGNONE, D. & VIÑALS, J. 1996 Two-phase binary fluids and immiscible fluids described by an order parameter. *Math. Models Meth. Appl. Sci.* **6**, 815–831.

HUH, E. & SCRIVEN, L. E. 1971 Hydrodynamic model of steady movement of a solid/liquid/fluid contact line. *J. Colloid Interface Sci.* **35**, 85–101.

INDEIKINA, A. & CHANG, H.-C. 1998 A molecular theory for dynamic contact angles. In *IUTAM Symp. on Non-Linear Singularites in Deformation and Flow*, pp. 321–337. Kluwer.

JACQMIN, D. 1995 An energy approach to the continuum surface tension method: application to droplet coalescences and droplet/wall interactions. Presented at the 1995 ASME IMECE, San Francisco, CA.

JACQMIN, D. 1996 An energy approach to the continuum surface tension method. *AIAA Paper* 96-0858.

JACQMIN, D. 1997 A variational approach to deriving smeared-interface surface tension models. In *Barriers and Challenges in Computational Fluid Mechanics* (ed. V. Venkatakrishnan & M. D. Salas), pp. 231–241. Kluwer.

JACQMIN, D. 1999 Calculation of two-phase Navier–Stokes flows using phase-field modeling. *J. Comput. Phys.* **155**, 96–127.

JASNOW, D. & VIÑALS, J. 1996 Coarse-grained description of thermo-capillary flow. *Phys. Fluids* **8**, 660–669.

KOPLIK, J. & BANAVAR, J. R. 1998 The no-slip condition for a mixture of two liquids. *Phys. Rev. Lett.* **80**, 5125–5128.

KOPLIK, J., BANAVAR, J. R. & WILLEMSEN, J. F. 1989 Molecular dynamics of fluid flow at solid surfaces. *Phys. Fluids* A **1**, 781–794.

KOTHE, D. B., RIDER, W. J., MOSSO, S. J. & BROCK, J. S. 1996 Volume tracking of interfaces having surface tension in two and three dimensions. *AIAA Paper* 96-0859.

LAFAURIE, B., NARDONE, C., SCARDOVELI, R., ZALESKI, S. & ZANETTI, G. 1994 Modeling merging and fragmentation in multiphase flows with SURFER. *J. Comput. Phys.* **113**, 134–147.

LI, D. & SLATTERY, J. C. 1991 Analysis of the moving apparent common line and dynamic contact angle formed by a draining film. *J. Colloid Interface Sci.* **143**, 382–396.

LOPEZ, J., MILLER, C. A. & RUCKENSTEIN, E. 1976 Spreading kinetics of liquid drops on solids. *J. Colloid Interface Sci.* **56**, 460–468.

LOWENGRUB, J. & TRUSKINOVSKY, L. 1998 Quasi-incompressible Cahn–Hilliard fluids and topological transitions. *Proc. R. Soc. Lond.* A **454**, 2617–2654.

MATSUMOTO, S., MARUYAMA, S. & SARUWATARI, H. 1995 A molecular dynamics simulation of a liquid droplet on a solid surface. *Proc ASME-JSME Thermal Engng Joint Conf., Maui*, Vol. 2, pp. 557–562.

MILLER, C. A. & RUCKENSTEIN, E. 1974 The origin of flow during wetting of solids. *J. Colloid Interface Sci.* **48**, 368–373.

NADIGA, B. T. & ZALESKI, S. 1996 Investigations of a two-phase fluid model. *Eur. J. Mech.* B/*Fluids* **15**, 885–896.

NGAN, C. G. & DUSSAN V., E. B. 1982 On the nature of the dynamic contact angle: an experimental study. *J. Fluid Mech.* **118**, 27–40.

POISSON, S. D. 1831 *Nouvelle Théorie de l'Action Capillaire*. Paris: Bachelier.

ROWLINSON, J. S. & WIDOM, B. 1982 *Molecular Theory of Capillarity*. Oxford University Press.

SEPPECHER, P. 1996 Moving contact lines in the Cahn–Hilliard theory. *Intl J. Engng Sci.* **34**, 977–992.

SUSSMAN, M., SMERAKA, P. & OSHER, S. J. 1994 A level set approach for computing solutions to incompressible two-phase flow. *J. Comput. Phys.* **114**, 146–159.

THOMPSON, P. A. & ROBBINS, M. O. 1989 Simulations of contact-line motion: slip and the dynamic contact angle. *Phys. Rev. Lett.* **63**, 766–769.

THOMPSON, P. A. & ROBBINS, M. O. 1990 Shear flow near solids: epitaxial order and flow boundary solutions. *Phys. Rev.* A **41**, 6830–6837.

UNVERDI, S. O. & TRYGGVASON, G. 1992 A front-tracking method for viscous, incompressible, multi-fluid flows. *J. Comput. Phys.* **100**, 25–37.

WAALS, J. D. VAN DER 1893 The thermodynamic theory of capillarity flow under the hypothesis of a continuous variation of density. *Verhandel. Konink. Akad. Weten. Amsterdam* **1** (English transl. by Rowlinson, J. S. in *J. Statist. Phys.* **20** (1979), 197–244).

WAGNER, L. 1995 Molecular dynamics simulations of polymer droplets. *Phys. Rev.* E **51**, 499–503.

WAYNER, P. C. & SCHONBERG, J. 1992 Spreading of a liquid film on a substrate by the evaporation–adsorption process. *J. Colloid Interface Sci.* **152**, 507–519.